Pure Appl. Geophys.

https://doi.org/10.1007/s00024-026-04051-7

Pure and Applied Geophysics

Full Waveform Inversion of DAS Crosswell Data to Monitor HT-ATES: A Synthetic Feasibility Study

Clara E. Fraile,[1] Emmanuel Gaucher,[1] and Christophe Barnes[2]

Abstract—Monitoring underground reservoirs is essential to ensure their efficient and sustainable operation. This study investigates the detectability and imaging, using seismic methods, of modifications in elastic properties caused by cyclic injection and production of geothermal fluid in high-temperature aquifer thermal energy storage (HT-ATES) systems. In such systems, the induced variations in elastic properties are expected to be very small, requiring high-sensitivity methods for reliable detection. The work is conceived as a feasibility study in a setting where field data are not yet available. Synthetic modelling is used to evaluate the effectiveness and sensitivity of Full Waveform Inversion (FWI) to reservoir variations. FWI is selected for its ability to exploit the full recorded wavefield, which is critical for resolving subtle elastic changes in thin, low-contrast reservoirs. The DeepStor HT-ATES research project in Karlsruhe, Germany, where layers thinner than 10 m at 1.3 km depth are targeted, serves as a case study. Two elastic models were developed: one unperturbed and one incorporating anomalies expected after five years of cyclic operations. Due to the thickness and depth of the targets, surface seismic methods were excluded in favour of cross-well configurations using Distributed Acoustic Sensing (DAS). Active sources are adopted to ensure controlled and repeatable illumination required for time-lapse monitoring. Results indicate that geometries with receivers intersecting the reservoirs significantly improve imaging and parameter estimation. This study evaluates the applicability of established FWI approaches in thin, stratified geothermal systems and highlights the importance of survey design for successful HT-ATES monitoring.

Keywords: Distributed acoustic sensing, inverse problem, numerical modelling, waveform inversion, reservoir monitoring.

1. Introduction

1.1. Geothermal Systems

Geothermal systems consist of three main components: a heat source, a reservoir and a fluid to transport the heat (Ganguly & Mohan Kumar, 2012). When the fluid flows through a porous medium, such as hot springs, aquifers or geysers, the system is classified as hydrothermal.

An example of hydrothermal systems is the Aquifer Thermal Energy Storage (ATES) system, an open-loop configuration, in which excess thermal energy is stored by injecting hot fluid into permeable underground layers during low demand periods (e.g., in summer) and recovered when the heat demand is high (e.g., in winter) (Ocłoń 2021; Stober & Bucher 2021; Stricker et al., 2020). ATES typically target shallow aquifers, which are more economically viable, and operate at temperatures below 50 °C (Banks et al., 2021). While temperatures are suitable for domestic use, they are insufficient for industrial or large district heating demands (Stricker et al., 2020).

To achieve higher temperatures, High Temperature (HT) ATES systems store heat at greater depths. Their high temperatures allow direct heat use, reducing the need for heat pumps and thereby enhancing the system efficiency. Furthermore, HT-ATES systems operate in deeper geological formations, without disturbing near-surface groundwater aquifers, and they can function at lower flow rates (Drijver et al., 2012; Stober & Bucher, 2021; Stricker et al., 2020).

In systems with fluid reinjection, such as ATES and HT-ATES, thermal equilibrium is rarely achieved (Chen et al., 2020). Temperature variations

[1] Institute of Applied Geosciences (AGW), Karlsruhe Institute of Technology (KIT), Adenauerring 20b, 76131 Karlsruhe, Baden-Württemberg, Germany. E-mail: clara.fraile@kit.edu; emmanuel.gaucher@kit.edu

[2] CY Cergy Paris Université, Sorbonne Université, CNRS, Institut des Sciences de la Terre de Paris, ISTeP, 95000 Cergy, France. E-mail: christophe.barnes@cyu.fr

Published online: 27 July 2026

influence the groundwater chemistry and the physical properties of both the surrounding rock and fluid (Cartagena-Pérez et al., 2018). Fluid pressure changes are equally important, as they influence processes such as heat flow and groundwater movement (Doetsch et al., 2018). In deep geothermal fields, pressure and temperature variations can also modify the geomechanical properties, potentially leading to ground deformation, subsidence, fault reactivation, micro-seismicity, and other geomechanical hazards (Chen et al., 2020). Hence, characterising the deep geothermal reservoir over time is vital to ensure the properties that led to its selection are not significantly altered and the overall system is sustainable.

1.2. Use of Seismic Methods for Geothermal Monitoring

Several geophysical methods are employed in geothermal monitoring (Azzola et al., 2023; Hermans et al., 2014; Hunt et al., 2009; Reinecker et al., 2021), with electromagnetic techniques often preferred due to their sensitivity to fluid content. Seismic methods are less commonly applied, mainly due to challenges such as poor data quality caused by background noise from power plants, rock heterogeneities, surface waves interference, reverberations and near-surface direct waves (Matsushima et al., 2004).

While seismic monitoring has proven effective in other subsurface applications, geothermal reservoirs present unique challenges due to the nature of the injected and in-situ fluids, which are typically both brines. In other geo-reservoirs, the seismic velocity contrast between initial and injected fluids is typically more pronounced. For example, injecting CO_2 into a brine-filled reservoir produces significant velocity changes due to the distinct mechanical properties of the fluids (Furre et al., 2017). Similarly, in oil and gas reservoirs, the contrast between hydrocarbons and water allows for effective monitoring of fluid migration using 4D seismic (Bjorlykke, 2010).

In geothermal reservoirs, since the fluid mechanical properties remain largely unchanged, velocity variations are primarily driven by pressure and temperature effects on the geomechanical properties of the medium. Thus, the seismic contrast between the system's initial and operational states is subtle. A key challenge in using seismic methods for geothermal storage is therefore detecting weak contrasts in different physical parameters, which requires highly sensitive seismic techniques capable of capturing small-scale changes in elastic properties.

Despite these limitations, seismic methods offer great potential for monitoring geothermal reservoirs. Their sensitivity to elastic moduli makes them responsive to changes in temperature, fluid pressure, stress, rigidity, and fluid saturation (Lowrie, 1997; Young et al., 2012). Additionally, their deeper penetration depth enhances subsurface imaging (Schmelzbach et al., 2016). Several studies have applied active seismic techniques in geothermal fields (Edwards et al., 2015; Matsushima et al., 2004; Rabbel et al., 2017), with a preference for Vertical Seismic Profiling (VSP) and cross-well survey to improve spatial resolution. However, seismic acquisition and processing techniques must be adapted to geothermal problems where very low impedance contrasts and weak reflection coefficients are typical (Schmelzbach et al., 2016).

1.3. Time-Lapse Monitoring

These characteristics make geothermal reservoirs a particularly challenging target for seismic monitoring: elastic-property changes are subtle, contrasts are weak, and the expected signals are below the noise level. Overcoming these limitations requires time-lapse active seismic approaches with repeatability, resolution, and sensitivity, specifically adapted to geothermal operating conditions.

Time-lapse monitoring is the process of acquiring and analysing multiple surveys, recorded at the same site, over time, to image fluid-flow effects in a producing reservoir (Lumley, 2001). The sensitivity of the 4D survey depends on its capability to detect small variations induced by fluid flow. Repeatability is crucial in the success of time-lapse surveys (Calvert, 2005), as minor changes in acquisition parameters, noise conditions, or near-surface properties can significantly affect the 4D seismic data (Bjorlykke, 2010; Calvert, 2005; Lumley, 2001). Consistent source, receiver, and processing parameters lead to high repeatability and help ensure that the observed changes are related to the reservoir evolution (Bjorlykke, 2010; Sambo et al., 2020).

Given the small pressure- and temperature-induced elastic changes expected in geothermal reservoirs, we selected a monitoring setup adjusted to geothermal conditions, prioritising high spatial resolution in depth and repeatability. Accordingly, passive seismic approaches such as ambient seismic noise tomography or interferometry are not considered due to low spatial resolution, sensitivity to the conditions of the near-surface layers and anthropogenic sources of noise, and because they are mainly limited to shear-waves (e.g. Cheng et al. (2021)). Although VSP is commonly employed, we opted for a cross-well geometry due to the scale ratio of more than 100 between the relatively large depth and the small thickness of the target layers that we will consider, which would make surface-to-borehole survey unsuitable. Also, in HT-ATES, the distance between wells is kept small (Sommer et al., 2015), making this survey geometry suitable. Downhole active seismic sources were chosen. As receiver network, we selected a fibre optic cable along which Distributed Acoustic Sensing (DAS) will be applied (Azzola et al., 2023; Cuny et al., 2024; Johannessen et al., 2012). DAS is one of the Distributed Optical Fibre Sensing (DOFS) methods, which captures the spatial distribution of the dynamic strain along a section of the fibre and is widely used in borehole seismics (Hartog, 2017). It provides high spatial and temporal resolution, making it suitable for monitoring purposes. Altogether, these characteristics make DAS in a cross-well active seismic configuration a promising candidate for monitoring reservoir variations induced by geothermal operations.

This study investigates the feasibility of time-lapse active seismic surveys using a cross-well DAS configuration to detect subtle elastic variations associated with fluid flow, temperature plumes, and potential leakage in underground heat storage systems. It considers a ratio greater than 100 between the depth of the reservoir layers and their thickness. The proposed approach consists of generating synthetic DAS data for baseline and monitor scenarios representative of geothermal operations and applying Full Waveform Inversion (FWI) employed as a high-resolution imaging tool to recover the elastic parameter changes. The use of noise-free synthetic data allows us to evaluate the detectability of these subtle variations under controlled conditions and to characterise the potential of the inversion method, under the most favourable conditions, before introducing additional complexities, which would constitute further work.

The FWI framework adopted here is based on established formulations from Tarantola (1984), incorporating specific constraints (Charara et al., 1996), to address the low elastic contrasts characteristic of geothermal reservoirs. This study focuses on the application and evaluation of such established FWI approaches in a challenging geothermal setting. Using synthetic data based on the geometry and mechanical properties of the DeepStor site (Karlsruhe, Germany), we evaluated different survey configurations, focusing on how acquisition geometry influences the detection, delineation, and estimation of elastic-parameter changes caused by geothermal operations.

1.4. Outline

Sect. 2 introduces the characteristics of the site, along with the properties of the baseline model (pre-operations) and the monitor model (during operations). Section 3 outlines the chosen FWI method, including its assumptions and numerical challenges. The results are presented and discussed in Sect. 4.

2. Case Study: DeepStor

2.1. Geological Context

The Upper Rhine Graben (URG), one of the oldest known oil provinces in the world (Böcker, 2015), has been extensively explored for hydrocarbon and geothermal energy. It is characterised by deep-reaching thermal anomalies mainly controlled by the distribution of unconsolidated Cenozoic rift sediments with very low thermal conductivity (Freymark et al., 2017; Stricker et al., 2020).

Based on this geological and thermal potential, the DeepStor site has been established at the KIT Campus North, near Karlsruhe, Germany. It will serve as a demonstrator for HT-ATES systems and as a research facility (Bremer et al., 2022). A test well will aim for the Meletta sandstone layers, targeting horizons with an estimated thickness close to 10 m and temperatures between 70° C and 80° C located at about 1300 m depth (Banks et al., 2021; Bremer et al., 2022). The system will inject hot fluid at an expected temperature of 140 °C, for six months, followed by six months of extraction, repeating this cycle over several years.

2.2. Conceptual Model

We constructed a synthetic velocity model based on the geological structure of the DeepStor site, designed to capture its main stratigraphic features and assess the sensitivity of time-lapse FWI to thin geothermal reservoir layers under realistic, yet idealised and controlled conditions.

The model includes two potential heat storage zones: a shallow zone (850–870 m) and a deep zone (1260–1305 m). However, this study focuses on the deepest zone. Both zones contain two reservoir layers whose thicknesses vary (12 m and 5 m in the shallow zone; 10 m and 6 m in the deep zone) to evaluate the FWI sensitivity to reservoir thickness in this acquisition geometry.

We assumed lateral homogeneity, and the small 5° eastward dip (Stricker et al., 2024) is neglected, resulting in a horizontal, parallel layering. Two vertical wells crossing the reservoirs are added to this conceptual model: one injection/production well, which will serve as the receiver well, and another one 100 m away, which will serve as the source well.

Two models were designed to test the FWI sensitivity to small elastic variations. The Baseline model corresponds to the initial state of the subsurface before geothermal operations, while the Monitor model introduces anomalies that correspond to the effects of expected pressure and temperature variation in the reservoirs. Both models share the same geometry but have different elastic properties within the reservoirs.

The Baseline model P-wave velocities (Fig. 1) are derived from a P-wave sonic log acquired south of Karlsruhe (Lutz & Cleintuar, 1999). The S-wave velocities were derived from borehole data and laboratory Vp/Vs ratio measurements. We used Gardner et al. (1974) equation to obtain the density. The geothermal target reservoirs are characterised by higher seismic velocities and lower densities than the surrounding layers, as shown in Table 1.

The Monitor model adds an anomaly for the three elastic properties (V_p, V_s, ρ) within the deep reservoirs (Fig. 2), based on preliminary thermo-hydro-mechanical simulations of the DeepStor operations (Fraile et al., 2024). These simulations assumed a single well alternating between injection in summer and production in winter. After 5 years of cyclic operation, an area of 30 m around the well is affected, with a maximum of 7% decrease in P-wave velocity and an increase of 0.1% in density. Hence, for the Monitor model, we applied a -7% variation for both P- and S-wave velocities, and a density variation of $+1\%$ uniformly within a 30 m radius around the well, which also serves as the receiver location.

2.3. Synthetic Inversion Experiments

We performed a feasibility study to assess the capabilities of FWI to image the planned DeepStor HT-ATES system. We evaluated its ability to detect and quantify the Baseline reservoir geometry and elastic values, and its ability to detect the small anomalies introduced in the Monitor model.

As DeepStor has not yet been drilled, there is no observed seismic data to compare with theoretical seismograms. The simulation parameters are based on the planned monitoring tools and well geometries. This section outlines the source and receiver characteristics, along with the simulation and inversion parameters.

A base case was designed to define the inversion processing flow. Given the target depth (1300 m), the thickness of the reservoir layers (10 m) and the distance between wells (100 m), a crosswell survey was selected. Instead of filtering the data to get different frequency content, as is typically done with real data, we performed simulations for each required central frequency (30 Hz, 60 Hz and 120 Hz). No noise is added to the data to evaluate the performance of the inversion under ideal acquisition conditions before considering additional complexities.

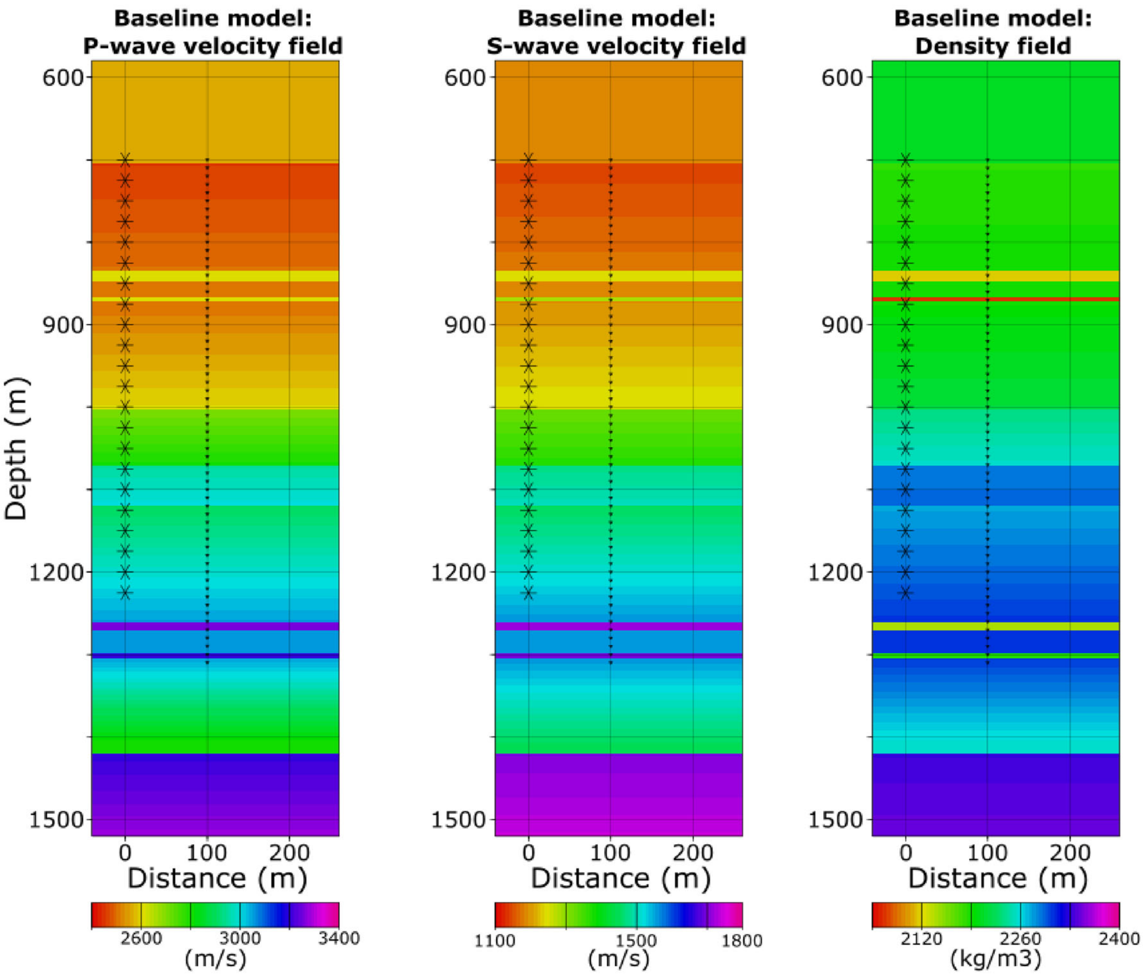

Figure 1
Baseline models for P-wave velocity (left), S-wave velocity (middle) and density (right). Each model presents the shallow zone, between 835 and 870 m, and the deep zone, between 1260 and 1305 m. Both zones have two thin reservoir layers. The asterisks correspond to the source locations, and the triangles indicate the receiver locations for the second geometry case (Case 2)

We tested several acquisition geometries, with sources and receivers spanning depths starting at 700 m. Simulations were performed by applying the elastic wave equation to the Baseline and Monitor models. Incorporating shear waves, the P- and S-wave scattered fields as well as their higher order interactions, enables the use of a larger portion of the seismogram compared to the acoustic case, providing additional constraints for the inversion. This enhances the resolution of subsurface imaging.

The experiments are conducted in a noise-free environment, without introducing geological complexities or acquisition errors, to assess the feasibility of applying DAS and FWI in an operational setting such as DeepStor. The problem is intentionally simplified to evaluate if crosswell-survey-based imaging is even possible under optimum conditions. Future work could account for these complexities.

2.3.1 Source Characteristics

The DeepStor project plans to use a downhole seismic vibrating source that generates both compressional and shear waves with a spherical radiation pattern for the P-waves and a toric pattern for the SH-

Table 1

Baseline and monitor elastic parameters for layers surrounding the deep geothermal reservoir

Depth	Layer	Baseline model			Monitor model		
		Vp (m/s)	Vs (m/s)	rho (kg/m3)	Vp (m/s)	Vs (m/s)	rho (kg/m3)
1120–1260	Cap	3050	1560	2304	3050	1560	2304
1260–1270	Reservoir	3250	1720	2141	3412	1806	2139
1270–1298	Cap	3070	1570	2308	3070	1570	2308
1298–1304	Reservoir	3200	1700	2182	3360	1785	2180
1304–1408	Cap	3050	1560	2304	3050	1560	2304

The model comprises three caprock layers and two reservoir layers

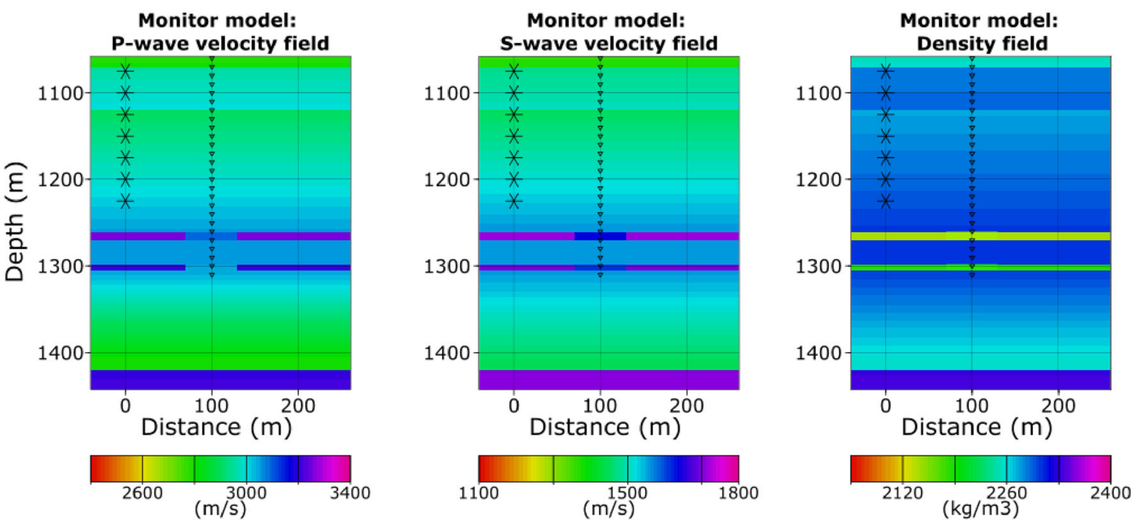

Figure 2

Monitor models. An anomaly with a radius of 30 m is added around the warm injection/production well, which is also the receiver well, in both deep reservoirs. The P- (left) and S-wave velocities (centre) decrease by 7%, while the density (right) increases by 1%

waves. The repeatability of the source would allow the recording of the emitted signal by the receivers.

For the numerical simulations, the source was simplified to reduce the problem from 3D to 2.5D. Hence, we simulate a stress source that generates both P- and S-waves with a Ricker wavelet, as it is a broadband, zero-phase source commonly used in numerical seismic studies. Its wide amplitude spectrum allows us to investigate the frequency-dependent behaviour of the FWI across the range of interest. The simulated source spacing was 50 m. The radiation pattern is nearly isotropic, with a slightly weaker ($\sigma_{ZZ} = 0.92$) energy released in the vertical direction than in the radial direction ($\sigma_{RR} = 1$), to reflect source-wellbore effects.

2.3.2 *Receiver Characteristics*

Since Distributed Acoustic Sensing was selected as the measurement method, the sampling points, distributed regularly, every 2.5 m along the fibre optic cable, constitute the "receivers". The DAS response is approximated by computing strain locally from the simulated wavefield, without explicit integration over a finite gauge length. As planned in the DeepStor project, the fibre optic cable is assumed vertical, cemented behind the casing of the monitoring well, making the receivers single-component vertical strain sensors. Cementation behind the casing will ensure good coupling to the formation and prevent seismic wave conversions associated with borehole effects (e.g., Stoneley waves).

DAS resolution is influenced by three elements: sampling resolution, spatial resolution and the gauge length (GL) (Hartog, 2017). The GL is particularly important when the seismic wavelength approaches its value, as DAS records strain integrated over the GL (Hartog, 2017; Lindsey et al., 2020). This integration introduces notches in the wavenumber response, behaving like an average filter in the spatial dimension (Hartog, 2017). These notches occur when the GL is an integer multiple of the acoustic wavelength.

Given the frequency range and velocities in this study, i.e the wavelengths, a conservative criterion of $GL < \lambda/4$ yields a maximum GL of 6.8 m for the P-waves, and 3.4 m for the S-waves. Besides, some studies suggest that the optimal GL is closer to $GL \approx \lambda/2$ (Cuny et al., 2024; Dean et al., 2017), as it is related to the signal-to-noise ratio. Hence, in our case study, with DAS every 2.5 m, the GL parameter was not considered as a limiting factor, especially as we are working with noise-free data and modern interrogators support gauge lengths smaller than 1 m.

2.3.3 Modeling Grid Parameters

The grid parameters were chosen based on the 10 m thickness of target layers and the Courant-Friedrichs-Lewy (CFL) criterion, ensuring numerical stability. We also followed the criteria of Virieux (1986) and assigned 10 grid points per wavelength to avoid numerical dispersion, considering the minimum S-wave velocity and maximum frequency. Hence, a spatial step of 0.8 m was used in both X and Z directions.

The model runs from 580 to 1550 m depth and covers a horizontal distance of 300 m, with the area of interest between 700 to 1450 m vertically and 0 to 100 m horizontally. The model is centred around the symmetry axis, which coincides with the location of the source well (see 3.1.1). Horizontally, the model starts 40 m to the left and ends 260 m to the right. The receiver well is located 100 m to the right of the axis. Absorbing boundaries are small at the axis location (3.2 m around the axis) and much thicker at the boundaries, reaching 120 m in the horizontal direction and 80 m at the top and bottom.

2.3.4 Survey Geometries

We evaluated four survey geometries by varying the maximum depth of sources and/or receivers, while keeping their spacing fixed (50 m for sources, 2.5 m for receivers). These geometries, shown in Fig. 3, test the effect of the positioning of the source and receiver relative to the depth of the deepest reservoirs to image: one where the last source and receiver are above the deep reservoirs (Case 1), at 1250 m, one in which both are below the deepest reservoir (Case 4) and two cases where either the receivers (Case 2) or the sources (Case 3) reach positions below the deepest reservoir.

3. Methodology

3.1. Full Waveform Inversion Method

Seismic full waveform inversion, introduced by Tarantola (1984), is a powerful imaging method that

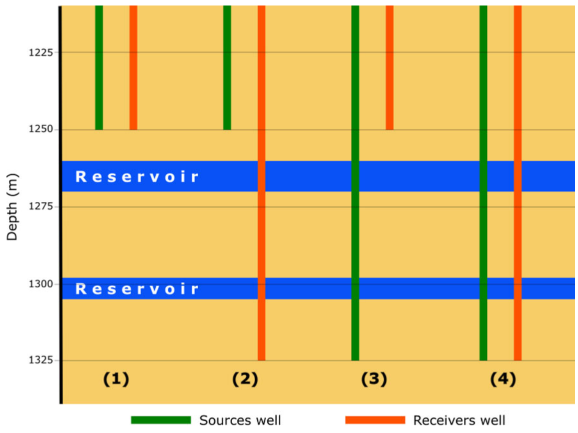

Figure 3
Schematic of the different evaluated geometries. (1) The deepest source and receiver are positioned above the first deep reservoir. (2) The deeper receiver is below the deepest reservoir, while the deeper source is above the first deep reservoir. (3) The deeper receiver is above the first deep reservoir, while the deeper source is below the deepest one. (4) The sources and receivers are distributed above, across, and below the deepest reservoir

considers all phases contained in the seismogram, such as multiple reflected energy, refracted energy and converted waves (Virieux et al., 2017). Using all this data makes it possible to achieve subsurface imaging with much higher resolution than with other seismic imaging methods (Virieux & Operto, 2009; Winner, 2023).

FWI aims to find a subsurface model that minimises the misfit between synthetic and observed waveforms (Fichtner, 2010). Numerical simulations of wave propagation based on an estimated model attempt to generate synthetic seismograms that are nearly identical to the observed ones. Hence, FWI involves two main steps: (1) the forward modelling, which computes the wave propagation for an estimated model, and (2) the inversion, which updates the model to improve the fit between the observed and the computed waveforms. For a more exhaustive description of FWI, see Virieux and Operto (2009) or Fichtner (2010).

3.1.1 Forward Modelling

The forward problem involves modelling the full seismic wavefield (Virieux & Operto, 2009) by solving the elastic wave equation:

$$\rho(\mathrm{x})\ddot{\mathbf{u}}_i(\mathrm{x},t) = \nabla_j \boldsymbol{\sigma}_{ij}(\mathrm{x},t) + \mathbf{f_i}(\mathrm{x},t) \tag{1}$$

where $\rho(\mathrm{x})$ is the density at point x, $\mathbf{u}_i(\mathrm{x},t)$ and $\ddot{\mathbf{u}}_i(\mathrm{x},t)$ are the i^{th} component of the displacement and acceleration at point x and time t respectively, and $\mathbf{f}_i(\mathrm{x},t)$ is the source term. The initial conditions at $t=t_0$ are $\mathbf{u}_i(\mathrm{x},t_0)=0$ and $\underline{\mathbf{u}}_i(\mathrm{x},t_0)=0$ and boundary conditions are either free surface conditions or absorbing conditions. Linear elasticity is assumed, such that stress $\sigma_{ij}(\mathrm{x},t)$ is related to strain $\varepsilon_{ij}(\mathrm{x},t)$ by:

$$\sigma_{ij}(\mathrm{x},t) = \mathbf{C}_{ijkl}(\mathrm{x})\varepsilon_{kl}(\mathrm{x},t) \tag{2}$$

where $\mathbf{C_{ijkl}}(\mathrm{x})$ denotes the fourth order stiffness tensor.

To represent DAS recordings, we follow the approach of Podgornova et al. (2022), which enables direct strain modelling by expressing displacement as a function of strain:

$$\varepsilon(\mathbf{u}) = \frac{1}{2}\left(\nabla\mathbf{u} + \nabla\mathbf{u}^T\right) \tag{3}$$

This method eliminates the need to convert strain to displacement.

We solve Eq. (1) using the Finite Differences method in the time domain, employing centred finite differences on a staggered grid (Virieux, 1984, 1986). Spatial operators are 4^{th} order, with coefficients optimised in the frequency domain. The time operator is 2^{nd} order with explicit time extrapolation.

Assuming axial (cylindrical) symmetry around the vertical source well, and DAS sampling points in the vertical receiver well recording only vertical strain the problem reduces to a 2D (r, z, t) formulation.

3.1.2 Misfit Function

After solving the forward problem, the subsurface model $\mathbf{m}$ is updated by minimizing the difference between observed ($\mathbf{d_{obs}}$) and predicted waveforms ($\mathbf{d_{pr}}(\mathbf{m})$), using a misfit function $\chi(\mathbf{m})$ (Fichtner, 2010; Virieux, 1986). Both datasets are generated with the same code (operator $\mathbf{G}$), eliminating potential inconsistencies from differences in numerical implementation, discretisation, or solver settings. This allows us to assess the FWI performance independently of any potential modelling-related errors.

We employ a weighted least-squares formulation to define the misfit function:

$$\begin{aligned}\chi(\mathbf{m}) = &\frac{1}{2}\left(\mathbf{G}(\mathbf{m}) - \mathbf{d}_{obs}\right)^{\top}\mathbf{C}_D^{-1}\left(\mathbf{G}(\mathbf{m}) - \mathbf{d}_{obs}\right) \\ &+ \frac{1}{2}\left(\mathbf{m} - \mathbf{m}_{pr}\right)^{\top}\mathbf{C}_M^{-1}\left(\mathbf{m} - \mathbf{m}_{pr}\right)\end{aligned} \tag{4}$$

where C_D and C_M are the data and model covariance matrices, which define the structure of the uncertainties in both spaces. Incorporating prior information to regularise the inversion helps prevent excessive oscillations in the model (Charara et al., 1996). The data covariance assumes 10% of the data mean amplitude as the amplitude uncertainties (per shot). The model covariance is described in detail in Sect. 3.1.3.

Gradient-based iterative methods are used to minimise the misfit function (Fichtner, 2010). These methods compute the derivative of the misfit function, χ, with respect to the model parameters and update the model iteratively. In this work, we adopt

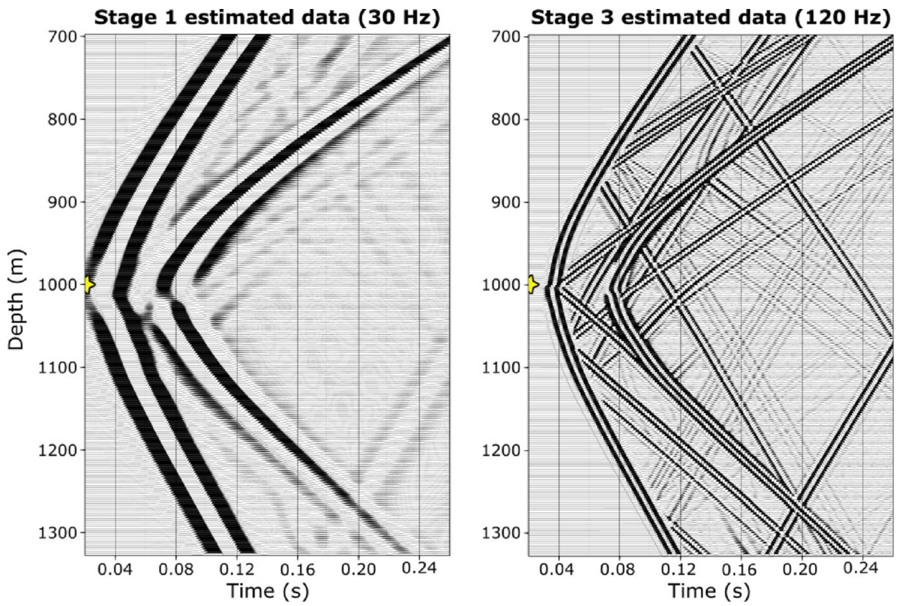

Figure 4
Comparison between Stage 1 (left) and Stage 3 (right) mid-depth seismograms. The amplitude corresponds to vertical strain along the fibre. In Stage 1, the source uses a low central frequency (30 Hz). In Stage 3, the source's central frequency is increased to 120 Hz, introducing more details and complexity to the data

Table 2
FWI stage parameters

Stage	Frequency (Hz)	Model	Gradient zone	Vertical correlation range (m)	Horizontal correlation range (m)
1	30	Baseline	Full area	13	1000
2	60	Baseline	Full area	5	500
3	120	Baseline	Full area	1.6	250
4	120	Baseline	Focused area	1.6	24
5	120	Monitor	Focused area	1.6	24
6	120	Monitor	Focused area	1.6	1.6

the *Conjugate Gradient* method, with the step length computed via linear search. For more details, please refer to Nocedal and Wright (2006) or Shewchuk (1994).

3.1.3 Model Constraints

Model constraints are introduced in the misfit function (Eq. (4)) through covariance matrices to stabilise the inversion. In this study, we focus on two types of constraints in the model space: spatial and algorithmic. We do not add constraints in the data space.

Spatial constraints like correlation range enforce smoothness by assuming that nearby points share similar properties. Given that in geological settings, layers tend to show higher horizontal symmetry, we enforce stronger horizontal smoothing, using an L2-norm laterally and an L1.5-norm vertically to account for increased vertical heterogeneity.

To account for uncertainties in the model, we adopt the approach of Charara et al. (1996), who added an algorithmic covariance to the misfit function. This term forces the algorithm to remain in regions where parameters are more spatially correlated, and has no effect once convergence is achieved. Introducing constraints reduces the degrees of freedom (Charara & Barnes, 2019), enforcing smoothing and helping stabilise the inversion process.

3.2. FWI Procedure

We implemented a six-stage FWI workflow to optimise the estimated model through multiparameter inversion, simultaneously estimating P-wave velocity, S-wave velocity and density. This section details the individual stages and their parameters. The four initial stages aim to recover the Baseline model, which is used as the true model, while the last two perform the inversion against the Monitor model.

At each stage, we propagate a seismic wave at a specific central frequency in the corresponding model to obtain the true data for the inversion. The first three stages aim to obtain a general image of the subsurface, while the last three focus on the target depths. To avoid cycle skipping, a known problem in FWI (Bunks et al., 1995; Cooper et al., 2021; Pladys et al., 2021), we gradually increase the frequency content, improving the likelihood of reaching the global minimum. Figure 4 compares results from the first (30 Hz) and the third (120 Hz) stages. The seismograms shown correspond to vertical strain measured along the fibre (DAS).

In addition, we progressively decrease the spatial correlation range at each stage (see Sect. 3.1.3) to reduce the number of parameters during inversion. In Stage 1, the horizontal range exceeds the lateral extent of the model, approaching near horizontal homogeneity. The inversion runs until the misfit reaches values below 1% (about 80 iterations for Stage 1). In the first stage, the initial model is a smoother version of the Baseline model, which will be discussed in Sect. 4.3. Each following stage uses the output model from the previous one as starting model, with updated frequencies and correlation ranges according to Table 2.

Although the high-frequency result of Stage 3 provides a good estimated model, higher accuracy is needed in the target zone to resolve the expected anomalies. Hence, in Stages 4–6, gradient calculations are restricted to the reservoir zone (1240–1320 m depth, 60–96 m horizontally). Stage 5 uses the same inversion parameters as Stage 4 but applies Monitor data instead of Baseline data. Finally, in Stage 6, the correlation range is further reduced to increase accuracy and sensitivity.

4. Results and Discussion

This section comprises four parts: (1) analysis of synthetic seismograms (true data) to examine the energy recorded at various receivers in response to the anomalies; (2) detailed description of Case 4, with sources and receivers extended below the deepest reservoir (see geometries in Sect. 2.3.4); (3) tuning of inversion parameters to optimise Case 3 results; and (4) comparison across all four cases.

The presented results should be interpreted within the controlled framework adopted in this study. The numerical experiments were conducted under noise-free conditions to evaluate the effectiveness of the survey design. Hence, the results present idealised scenarios intended to evaluate the feasibility of the approach, without accounting for complexities expected in real-field applications.

4.1. Synthetic Seismograms

To design the optimal acquisition geometry, we need to understand how the seismic energy from the sources propagates through the deep reservoirs and the surrounding media. Figure 5 shows shot gathers from the Baseline model for Shot 20 (1175 m depth, above the first reservoir), Shot 24 (1275 m depth, between both reservoirs) and Shot 26 (1325 m depth, below the deepest reservoir) using a 120 Hz source. The seismograms are normalised by shot and amplitude thresholds are applied to highlight different energy levels. Cases 4 and 2 record over 250 channels ("receivers"), while Cases 1 and 3 record over 220 only. This difference is indicated by the dotted line in the subplots of Fig. 5.

Figure 5 illustrates how the recorded wavefield strongly depends on the source position relative to the reservoir. When sources are located above the reservoir (e.g., Shot 20), most of the energy is

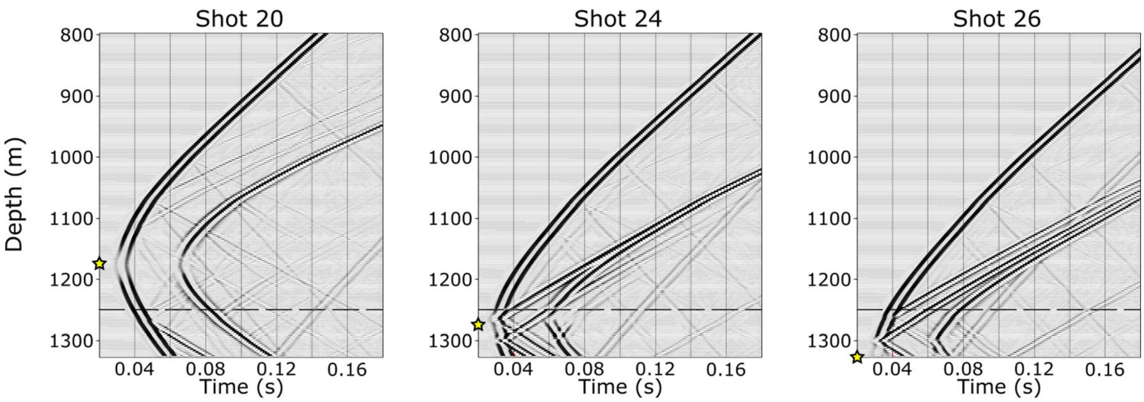

Figure 5
Shot gathers in the Baseline model for three source positions: Shot 20 (1175 m depth, above the first deep reservoir, column 1), Shot 24 (1275 m depth, between both deep reservoirs, column 2) and Shot 26 (1325 m depth, below the deepest reservoir, column 3). The amplitude corresponds to vertical strain along the fibre. The wavefields are dominated by direct arrivals, with weaker reflected and converted phases visible depending on the source position relative to the reservoirs. The dotted line indicates the end of the antenna for Cases 1 and 3

concentrated in the direct waves, reflecting the limited number of diffraction sources and the absence of strong impedance contrasts in the propagation path. In this configuration, converted and reflected phases have very low amplitudes, particularly above the reservoir, indicating that, in cases 1 and 3, much of the potentially informative signal is not recorded. The relatively simple wavefield also highlights the directional sensitivity of DAS measurements, which leads to near-zero amplitudes at the source depth for

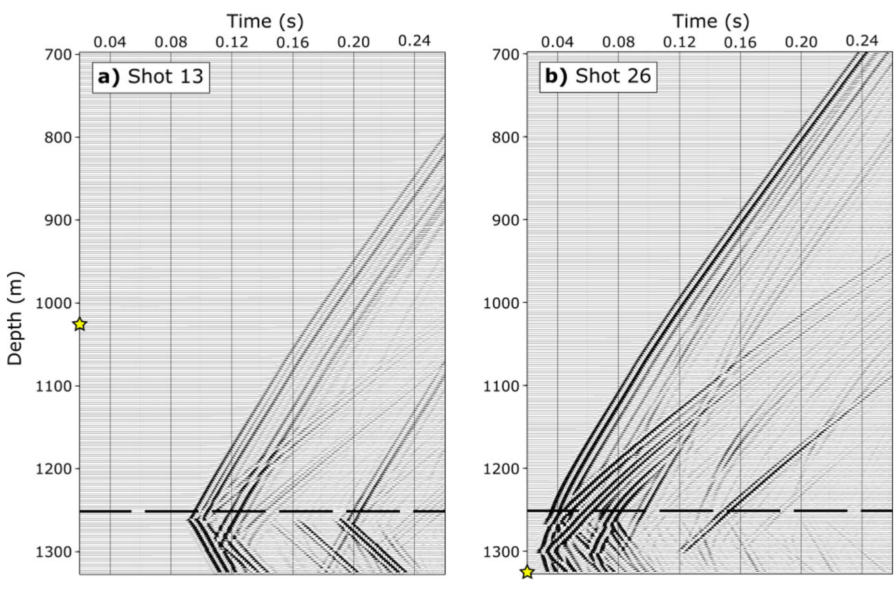

Figure 6
Shot gather difference between Baseline and Monitor for a shot above the reservoirs (Shot 13, left) and a shot below the deepest reservoir (Shot 26, right). The dotted line indicates the end of the antenna for Cases 1 and 3. The amplitude corresponds to vertical strain along the fibre. Most signals are recorded at the lower receivers, emphasising the importance of sampling at reservoir levels. The increased complexity of the seismograms better constrains the inverse problem, leading to improved inversion results. Both seismograms are plotted with the same amplitude threshold

orthogonally propagating P-waves and for shear forces associated with S-waves.

In contrast, when sources are placed at or below the reservoir (Shots 24 and 26), the wavefield becomes significantly more complex. P-to-S converted waves generated at the reservoir interfaces are clearly identifiable after the direct arrivals and may interfere with direct S-waves at larger offsets. At shallower depths, both P-wave reflections and additional converted phases are observed. Among the analysed configurations, Shot 24 exhibits the richest wavefield, whereas some of these features are weaker or absent in Shot 26. Overall, these observations demonstrate that placing sources and/or receivers at or below the target depths is essential to generate sufficient wavefield complexity for reliable FWI of reservoir variations.

To assess the effects of the geothermal operations, we calculated the difference between the Baseline and the Monitor synthetic seismograms (true data). Two source locations were analysed: Shot 13 (centre) and Shot 26 (below deepest reservoir). Figure 6a shows the difference for Shot 13, which has a normalised residual energy (seismic energy of the difference divided by the energy of the baseline seismogram) of 0.21%, with low-amplitude P-waves and some P-to-S waves reaching 1050 m. Higher amplitudes appear in the lower section, indicating greater waveform differences, mostly from P-to-S waves. This suggests that transmitted waves are more sensitive to anomalies than reflected ones.

For Shot 26 (Fig. 6b), the wavefield differences are more complex as the source is located closer to the reservoir, with a higher normalised residual of 1.8%. High amplitudes are predominantly in deeper channels, though some converted waves reach depth as shallow as 950 m. The upper section contains a greater variety of wavetrains, including direct and transmitted P-waves, and P-to-S waves with greater energy than in Shot 13, highlighting the importance of transmitted waves in this setting. Due to the proximity to the lower fibre section, Shot 26 displays multiple waveforms within a short time window, highlighting significant differences between the baseline and the monitoring shot gathers.

Figure 6 demonstrates that placing sources below target depths increases wavefield complexity and sensitivity to reservoir variations. This geometry allows shallower receivers to capture transmitted waves while increasing the complexity in deeper sections, which improves constraints for inversion, leading to more reliable results.

4.2. *Reference Survey Design*

According to the previous results, Case 4 (Fig. 3) presents the ideal survey geometry, with sources and receivers deployed above and below the reservoir layers. This configuration constitutes the reference survey design for evaluating the performance of FWI.

4.2.1 *FWI of Baseline Model*

Figures 7, 9, and 10 show the evolution of P-wave velocity, S-wave velocity and density inversion, respectively, across the six stages of the FWI for Case 4. Each profile includes the initial, true, and estimated models, along with receiver depth ranges. Profiles are taken 20 m from the receiver well to represent average values, as the anomaly spans 30 m and the gradient zone begins 4 m from the well.

In the first three stages of the P-wave velocity inversion (Fig. 7), the estimated model closely agrees with the true model at receiver depths. Both reservoir zones (800 m and 1260 m) are well recovered even at low frequencies. The agreement weakens below the fibre, however, the unconformity at 1400 m is still detected.

At Stage 1 (30 Hz), key features are already visible. The four reservoir layers are detected, with the shallow reservoir zone correctly located, and the deep reservoir zone slightly shallower. The section between 1100 m and 1260 m is the least stable, showing many oscillations in the estimated model. Below the fibre, the model accurately detects the sharp velocity change at 1400 m.

Before advancing stages, misfit values and model resemblance must be evaluated, since the algorithm can become trapped in local minima. In field acquisitions, where a true model is not available, geological data (e.g., structural maps, sedimentological columns, check-shots) can help assess model accuracy. This is particularly relevant at low-frequency stages, where data primarily capture large-

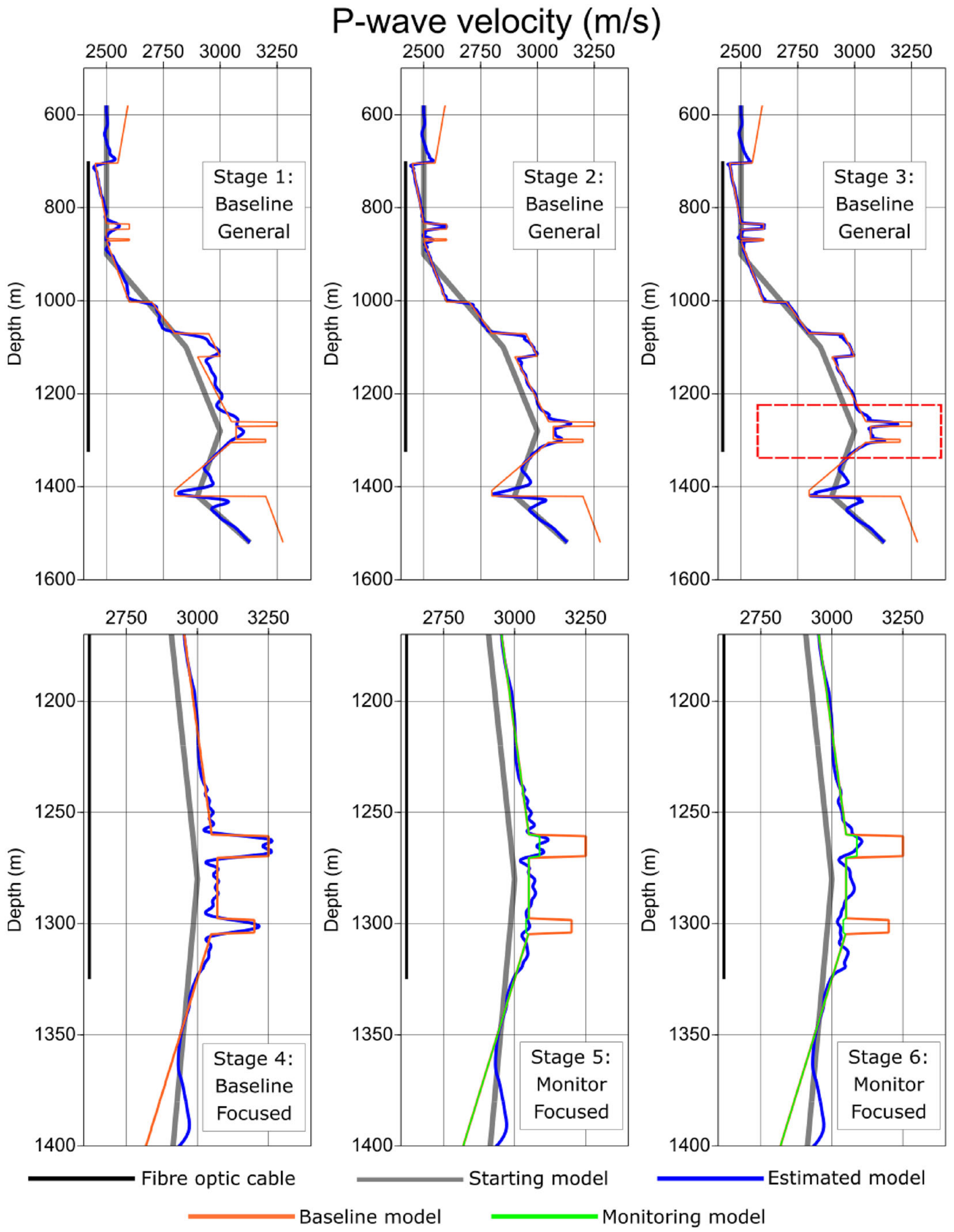

Figure 7
Case 4. Evolution of the FWI results as a function of the inversion stages. Each profile shows the depth range along which the receivers are deployed (black), the initial P-wave velocity model profile (grey), the estimated model (blue) and the Baseline model (orange). For Stages 1–4, the estimated model targets the Baseline model. From Stage 4 (bottom row), the gradient is calculated only around the deep reservoir zone. The depth interval of the deep reservoir, indicated by the red box in Stage 3, defines the region where the gradient is restricted from Stage 4 onward (bottom row). For Stages 5 and 6, the estimated model targets the Monitor model, displayed in green. Detailed information for each inversion stage is provided in Table 2

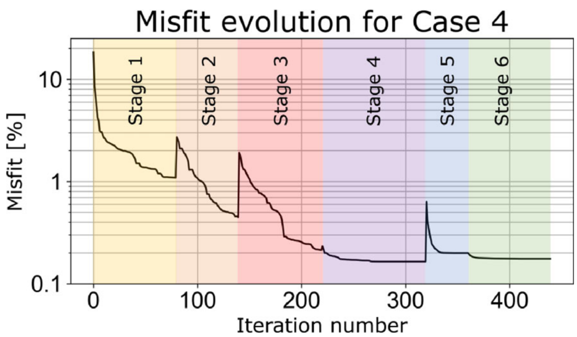

Figure 8
Evolution of the FWI misfit for the Case 4 geometry. In Stages 2, 3 and 5, new information is added to the inversion, causing an initial increase in misfit at the beginning of each stage before further reduction due to the introduction of new observed data. Convergence rates vary across stages, with Stages 4 and 6 showing the smallest misfit variations as they focus on refining the previously estimated model with no new data added

scale underground structures. At these stages, a broad geological model is sufficient to guide the inversion process.

Applying this methodology, we assessed the inversion of Case 4. After 80 iterations for Stage 1 (30 Hz, wavelength of 96 m), the misfit was 1.1%, and the estimated model agreed with the true data. This model was then used as the initial model for Stage 2 (60 Hz, average wavelength of 47 m), refining smaller-scale features while preserving large-scale structures and reducing the risk of local minima.

When increasing the frequency in Stages 1, 2, 3 and 5, the data volume grows, leading to an increase in the misfit at the beginning of each stage, as shown in Fig. 8. At the end of Stage 2, the misfit nearly stopped decreasing at a value of 0.45% around iteration 55. Some additional iterations confirmed this behaviour and the stage was stopped at iteration 60. The new estimated model corrected the depth of the deep reservoir zone, improved the resolution, and reduced the oscillations in the 1100–1250 m interval.

At Stage 3 (120 Hz, wavelength of 24 m), the upper layers and the deep reservoirs (10 m and 6 m thick) are well defined. The last stage of the Baseline model (Stage 4) only focuses on the depths shown in the lower row of Fig. 7. This focus improves the recovery of the P-wave velocity, detects the correct values and thicknesses in both deep reservoirs and further reduces the inversion misfit.

For S-wave velocity (Fig. 9), the model already fits the deep reservoirs by Stage 2, with fewer oscillations than in the P-wave model. By Stage 3, all layers are accurately positioned; however, the velocities of the deep reservoirs are overestimated. Below the fibre, the model cannot detect the unconformity and follows the initial model trend. Stage 4 correctly recovers the velocity values at the reservoirs. Overall, the S-wave model converges faster and more accurately at fibre depths.

Figure 10 shows that the density inversion is less accurate, a well-known issue in seismic inversion (Virieux & Operto, 2009). While all interfaces are detected, it fails to reach the absolute value of the deep reservoir layers. Nevertheless, the thicknesses and locations agree with the true model, and the contrasts are preserved.

The final inversion misfit of the Baseline model for Case 4 geometry is 0.16%. This corresponds to Stage 4 and accounts for the three model parameters: density, P- and S-wave velocity.

4.2.2 FWI of Monitor Model

As described in Sect. 2.2, the Monitor model introduces a -7% change in P- and S-wave velocities and +1% variation in density within a 30 m radius from the receiver well in the deep reservoir zone.

Figure 8 shows a high misfit increase at the start of Stage 5 associated with the introduction of the new data. The misfit value rises from 0.16% (end of Stage 4) to 0.63% at the beginning of Stage 5, and drops to 0.2% by the end of the stage. The inversion successfully detects the velocity decrease at the reservoirs (Figs. 7 and 9, respectively), recovering the magnitudes and thicknesses correctly, confirming the sensitivity to the anomaly.

In Stage 6, the P- and S-wave velocity profiles appear smoother and agree with the true model. Given the higher degrees of freedom in this stage, some oscillations are expected. This may explain the observed increase in P-wave velocity just below the deepest reservoir, unless it is associated with numerical noise or the illumination limitations.

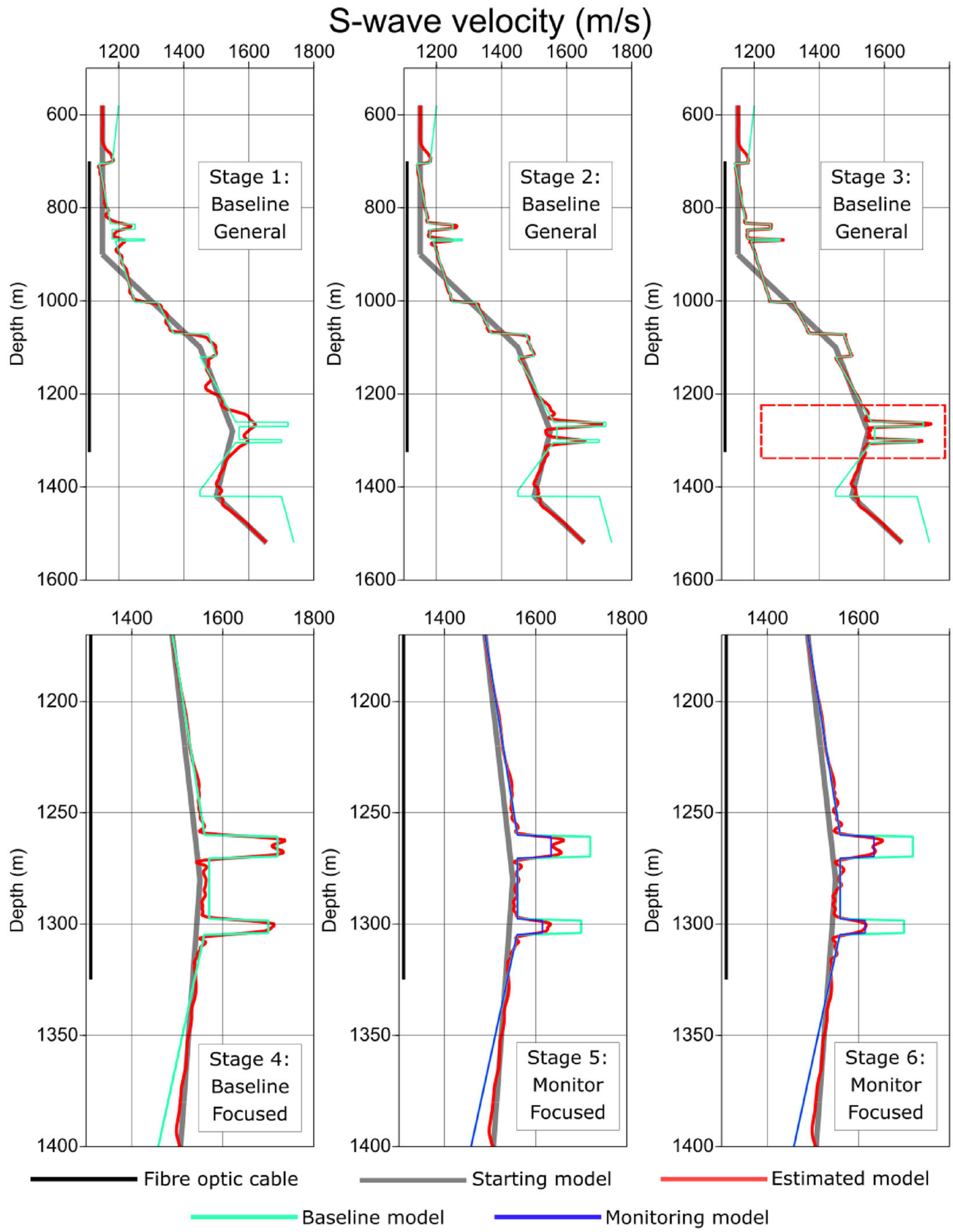

Figure 9
FWI cycle for the S-wave in Case 4, following the same inversion strategy and stage sequence as in Fig. 7. Profiles show the DAS fibre deployment (black), the initial model (grey), the estimated model (red), and the Baseline (turquoise) or Monitor (blue) model, depending on the inversion stage. The red box indicates the depth interval where the gradient is restricted from Stage 4 onward

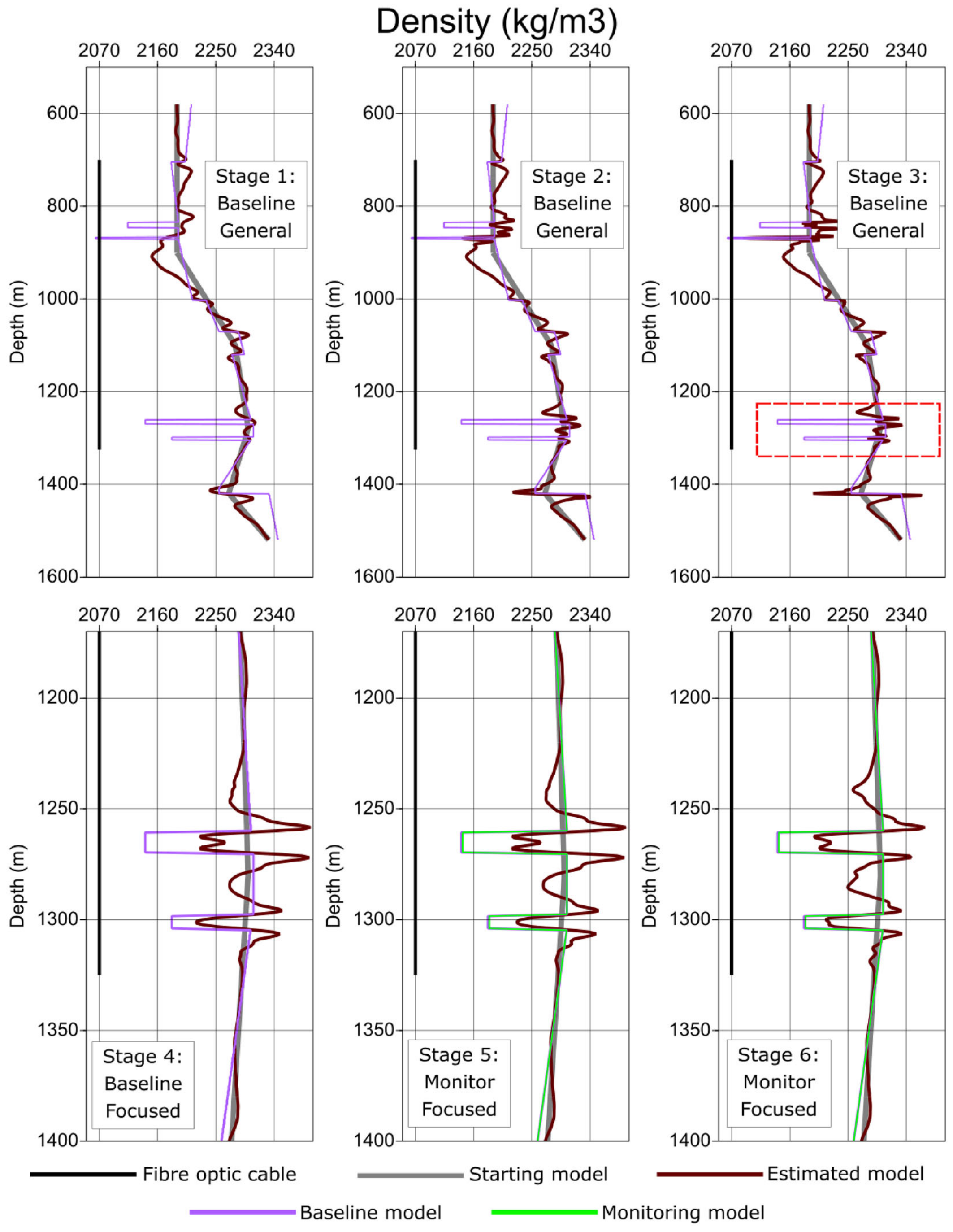

Figure 10
FWI cycle for the density in Case 1, following the same inversion stages and workflow as in Fig. 7. Profiles show the DAS fibre deployment (black), the initial model (grey), the estimated model (brown), and the Baseline (lilac) or Monitor (green) model. The red box in Stage 3 marks the depth interval used for gradient restriction from Stage 4 onward

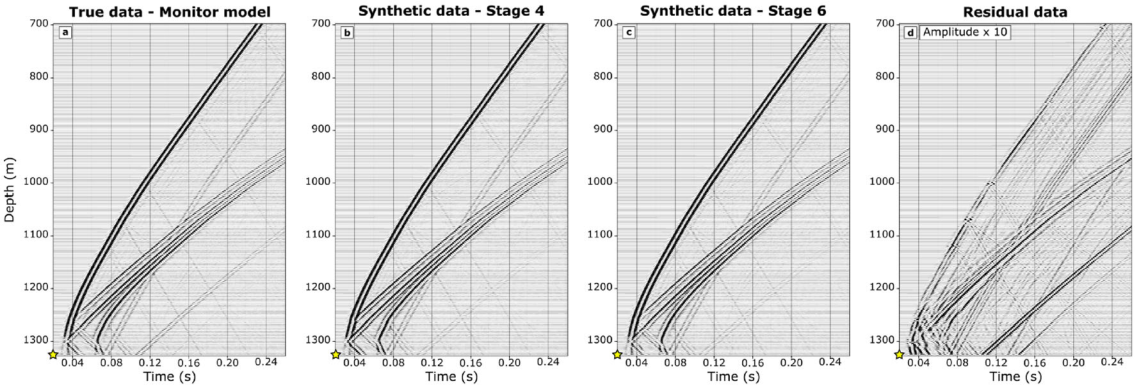

Figure 11

Comparison between seismograms for shot 26 (1325 m): true data from the Monitor model (a), synthetic data from the Baseline model at Stage 4 (b), synthetic data from the Monitor model at Stage 6 (c), and Monitor model residuals at Stage 6 (d). The amplitude corresponds to vertical strain along the fibre. For visibility purposes, the amplitudes of the residuals have been multiplied by 10. The low energy of the residuals indicates strong agreement between the true and synthetic data

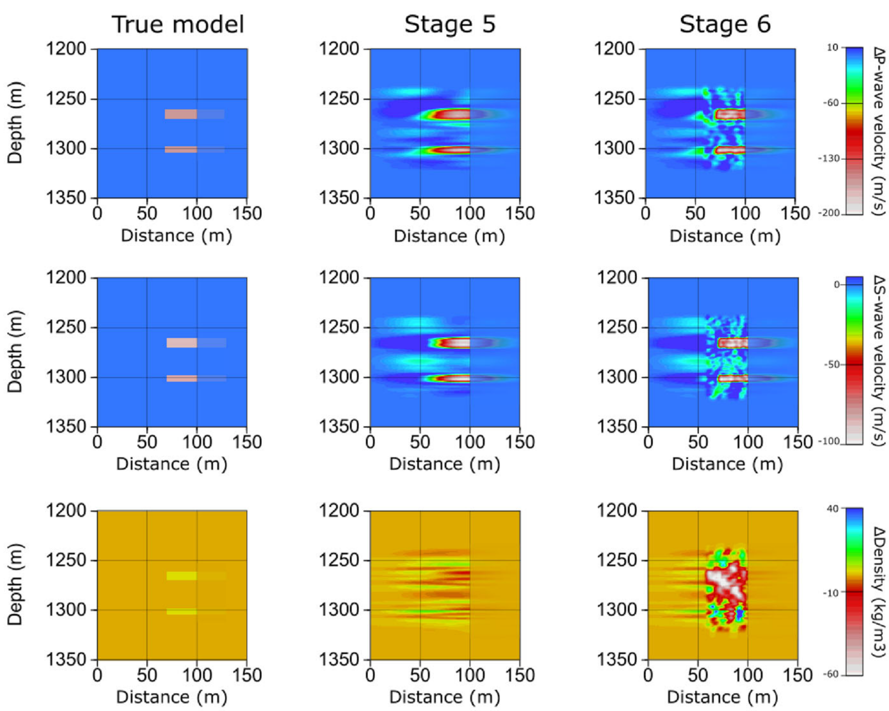

Figure 12

Differences between the Monitor model and the Baseline model. The left column shows the true anomaly used for the simulations. The middle and right columns show the anomalies obtained by FWI after Stage 5 and Stage 6, respectively, expressed as differences relative to Stage 4. Results are shown for the three elastic parameters: P-wave velocity (top row), S-wave velocity (middle row) and density (bottom row)

Regarding density, the 1% variation between the Baseline and Monitor models produces minimal differences. Stage 5 (Fig. 10) shows no significant changes. However, in Stage 6, as parameters are less constrained, the shape of the layers varies. At the reservoirs, the density decreases and the mismatch with the true one is reduced.

The final misfit for the Monitor model, for Case 4, at Stage 6, is 0.17%, which is very close to the misfit for the Baseline model. As shown in Fig. 11, the synthetic seismograms closely reproduce the main phases of the wavefield, with only low-amplitude residuals.

Figure 12 shows the differences between the Monitor and the Baseline models for the true models and those obtained from Stage 5 and Stage 6, for the P- and S-wave velocities and the density across the plane between the sources and the receivers. The anomaly appears on both sides of the receiver well, but given the acquisition geometry, inversion was carried out only between the sources and the receivers. Hence, the area to the right of the receiver well was not updated and should be disregarded.

At Stage 5, the anomalies are correctly detected for all three parameters and relatively well resolved in depth for the velocity anomalies. However, their extent is overestimated due to the large correlation range. Stage 6 illustrates how reducing the correlation ranges, based on an already reliable model, improves the resolution of the geometry of the velocity anomalies. However, the values are slightly overestimated and numerical noise increases around the deep reservoirs. Updates are confined to the focused area (70–96 m horizontally).

In contrast, density is more difficult to recover and highlights the consequences of increasing the number of degrees of freedom in areas that do not have a good initial model (i.e., Stage 4). The small variation (+1% or 2 kg m^{-3}) is difficult to constrain, especially in depth. Stage 5 exhibits many layers not present in the True model, although some signals can be identified in the upper reservoir. Stage 6 recovers part of the geometry of the upper reservoir anomaly, but features in the deepest reservoir remain unclear. Overall, the density change amplitude is not recovered.

4.3. *Initial Model and Prior Uncertainty*

Case 4 has the best illumination and the largest amount of data, resulting in a smooth inversion process that required few constraints to reach convergence. This was not the case in other geometries, where the limited illumination made the inversion process more challenging.

In Cases 1 and 3, the fibre does not reach the deep reservoirs, resulting in missing wavetrains and poor model recovery, even at low frequencies. Indeed, only one phase (reflected or transmitted, depending on source position) carries reservoir information. Additionally, longer travel paths increase energy losses, especially when crossing the reservoirs.

As a result, FWI in Cases 1 and 3 incorrectly defined a high-velocity layer from 1100 to 1200 m, rather than resolving the thinner layer at 1100 m depth (Fig. 13a). We verified the absence of cycle skipping, confirming the model was trapped in a local minimum.

In cases where the seismic waveform content is insufficient to constrain the inversion, parameters such as the initial model or prior information become critical. Case 3 showed the highest sensitivity to the initial model and the largest misfit. We therefore analysed how variations in model prior uncertainties and initial models affect the FWI results and illustrate the results for Case 3.

The true model contains four high-velocity zones: shallow reservoirs at 850 m, a layer between 1100 and 1150 m, deep reservoirs at 1260–1305 m, and an unconformity at 1400 m. We focused on the first three. Starting model A (grey line in Fig. 13a), also used in Case 4, is a smoothed version of the true model. The initial models and uncertainties shown in Fig. 13 correspond to the P-wave velocity. Similar behaviour was considered for the S-wave velocity and the density.

The top row in Fig. 13 shows the evolution of the P-wave velocity model estimated after incorporating uncertainties and refining the initial model. Using the Starting model A with constant uncertainties (Fig. 13a and d), the inversion barely detected the first high-velocity zone, extended the second layer and gave it higher values, and missed the deep reservoirs entirely. The model did not update below 1250 m. The large high-velocity layer at 1000 m depth likely results from high-velocity features present in the True model combined with the FWI's inability to accurately locate their source due to insufficient sampling below the fibre (1250 m). The algorithm compensates by artificially increasing

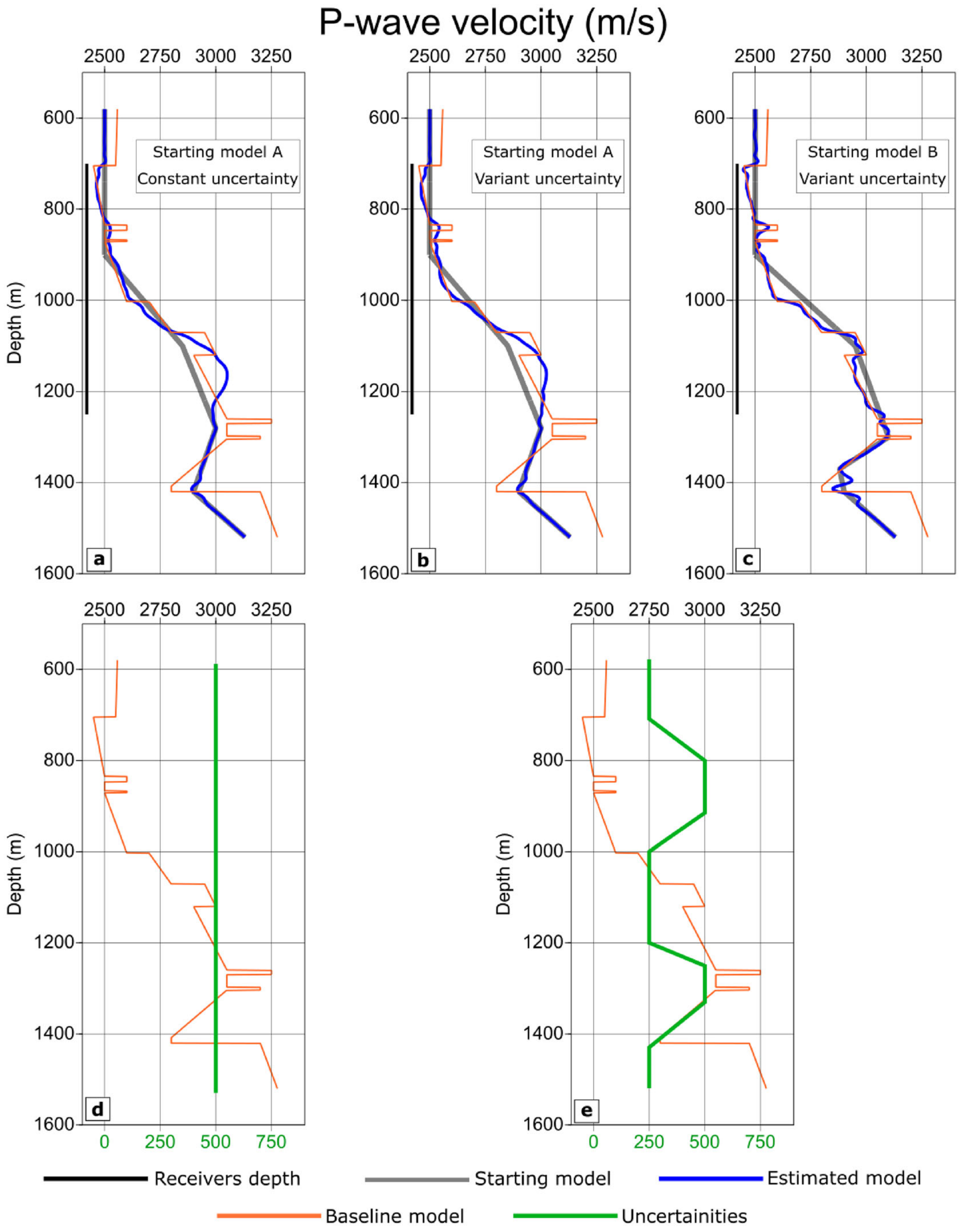

Figure 13
Case 3. Effects of the P-wave velocity initial model and prior uncertainties in the convergence of the estimated model (a, b and c) towards the true model (Stage 1). The variation of prior uncertainty on the initial model from (d) to (e) makes the algorithm focus on specific depth ranges and improves the results from (a) to (b), respectively. Increasing the prior model uncertainties only at the reservoir levels (e) makes the high-velocity anomaly less prominent and the shallow reservoir zone is better resolved (b). The updated Starting model B (see text for details) (c) allows the estimated model to fit the main features of the true model. The same variations and depths were considered for the S-wave velocity and the density

velocities near the end of the fibre to fit the observed data.

To address these limitations, we introduced uncertainties into the model space (Fig. 13e), identifying intervals that should align with the initial assumptions and those that may require more updates. We doubled the uncertainties in the proximity of the reservoirs. This adjustment, shown in Fig. 13b, led to a better detection of the shallow reservoir zone and a better fit of the central high-velocity zone. The misfit dropped from 2.6% (Fig. 13a) to 2.1% (Fig. 13b) by iteration 30 and continued to decrease. We adopted these uncertainties across all six stages of the FWI and all four cases.

Despite improvements, the estimated model still differed significantly from the true model. To achieve a better fit, we tested several initial models, focusing on depths below 1000 m. Increasing the model complexity by adding control points near the bottom and steeper velocity gradients yielded better results.

Starting model B (grey line in Fig. 13c) used higher velocities and introduced a larger variation at 1440 m. Fitting from overestimated velocities proved to be easier than adjusting from lower values, as in Starting model A. This may be because by starting with higher velocities, different sections of the observed data provide conflicting signals, where some sections require an increase in velocities and others a decrease, allowing the inversion to identify interfaces more accurately. Using the Starting Model B and the adjusted uncertainties (Figs. 13c and e), the inversion successfully detected all four high-velocity zones, even at low frequencies. After 35 iterations, the misfit reached 1.04%, agreeing with the main structures of the estimated model, and we proceeded to Stage 2.

It is well established that an initial model must be sufficiently close to the true subsurface model to increase the likelihood of converging to the global minimum (Tarantola, 1984; Virieux & Operto, 2009). Additionally, the introduction of *a priori* information and constraints provides numerical stability (Charara et al., 1996; Pratt et al., 1998). The results presented here reinforce these principles, especially in Cases 1 and 3, where limited waveform content and poor spatial sampling make the inversion process more challenging. In such scenarios, a carefully selected initial model and well-defined uncertainty estimates are even more critical.

4.4. Acquisition Geometry Comparison

To assess the impact of acquisition geometry on imaging, Figs. 14 and 15 show P- and S-wave velocity inversion results at Stage 4 and Stage 6, respectively, across the four geometries, for depths below 1200 m. In both figures, the top row shows the P-wave velocity, and the bottom row displays the S-wave velocity. As in Fig. 7, profiles are taken 20 m from the receiver well.

In the Baseline model (Fig. 14), Case 1 struggles the most, detecting only the upper reservoir. Case 2 recovers both layers, though slightly underestimates the deepest reservoir velocity and overestimates the intermediate layer. Case 3 accurately retrieves thicknesses and depths, but the magnitudes of the P-wave velocity differ from the true model. Also, it exhibits more oscillations, suggesting instability in the inversion process. Case 4 (discussed earlier) shows the best fit, with the correct depth, thickness and velocity values, and minimal artefacts.

S-wave inversion (bottom row in Fig. 14) generally performs better. Case 1 detects both reservoirs and resolves the upper one better. Case 2 has a slightly more accurate fit than its P-wave equivalent. Case 3 shows improved velocity recovery for both deep reservoirs, but although the magnitude at the deepest reservoir is inaccurate, its contrast with the surrounding layers is well represented. Finally, Case 4 matches the P-wave inversion but with fewer oscillations. The comparison between P- and S-wave results highlights the added value of recording elastic waves for resolving thin layers.

Figure 15 presents the results for the Monitor model, simulating geothermal-induced variations: 7% decrease in P- and S-wave velocity (-160 m s^{-1} and -85 ms^{-1}) and a 1% increase in density ($+2$ kg m^{-3}) affecting a 30 m radius around the receiver well in the deep reservoir layers.

The deepest reservoir in the Monitor model has a P-wave velocity very similar to the surrounding layers, making its detection challenging due to the small contrast. This difficulty is evident across all cases, shown in the upper row of Fig. 15. While all

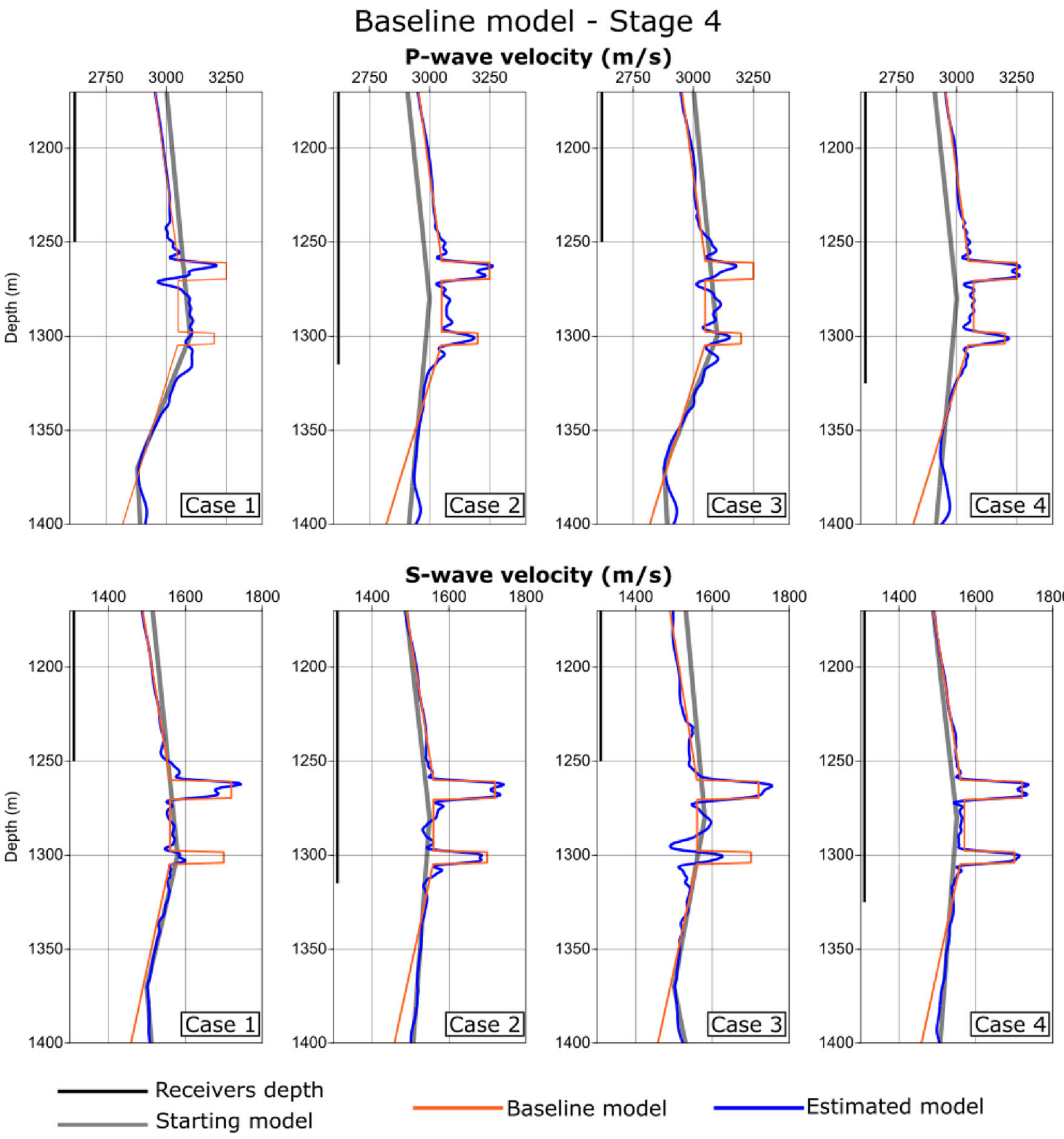

Figure 14
Comparison of the true (orange) and estimated (blue) Baseline models at the end of Stage 4 for all acquisition geometries. The profiles are taken 20 m from the receiver well. The top row shows the P-wave velocity results and the bottom row shows the S-wave ones. The top reservoir is detected by all geometries; however, only Cases 2 and 4 recover its amplitude in both P- and S-waves. The bottom reservoir is detected by Cases 2, 3 and 4 in the P-wave model, and in all geometries in the S-wave model. Only Cases 2 and 4 successfully detect and recover the correct amplitude of the bottom reservoir

four cases detect a velocity decrease, they also introduce an artificial layer between the reservoirs. On the contrary, the S-wave velocity contrast (bottom row) between the reservoirs and surrounding layers is stronger, improving the differentiation of the layers and, therefore, the inversion results.

In Case 1, the limited data coverage, combined with a high number of degrees of freedom, causes the inversion to become trapped in local minima, leading

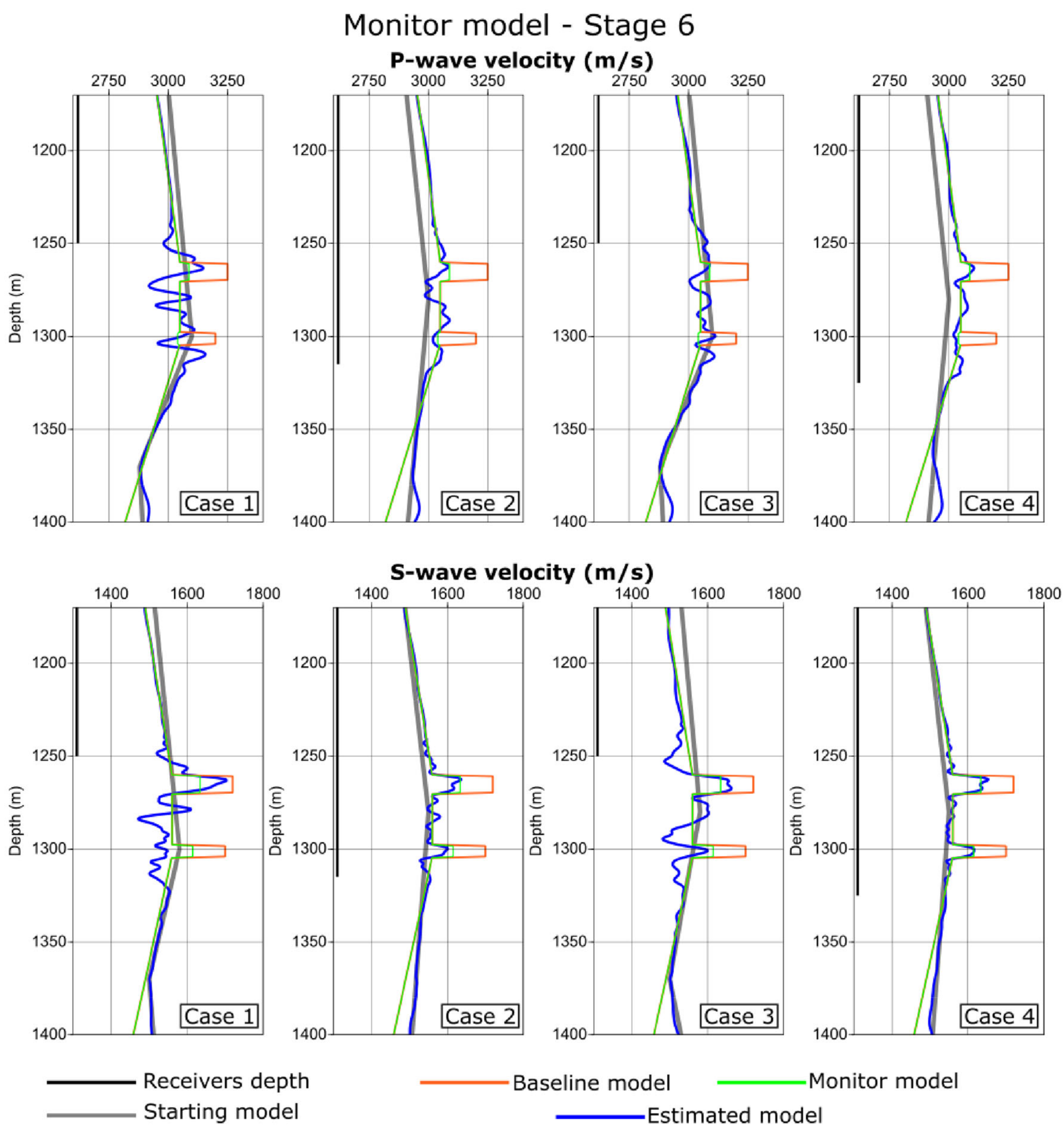

Figure 15
Comparison of the true (green) and estimated (blue) models for the Monitor model at the end of Stage 6 for all cases. The Baseline model (orange) is added for reference. The estimated model should be representative of the Monitor model at the end of this stage. The profiles are taken 20 m from the receiver well. The top row corresponds to P-wave velocity results, the bottom row shows S-wave velocity results

to the creation of non-existent layers. Moreover, Case 1 already failed to represent the Baseline model (Stage 4), making it even more challenging to achieve convergence for the Monitor model. Still, a general velocity decrease is detected.

Case 2 performs better: the P-wave velocity captures the velocity decrease, although the upper reservoir thickness is incorrect, and an additional layer appears. The S-wave profile, however, has a good agreement with the true model. Case 3 contains some artificial layers and fails to capture the reservoir

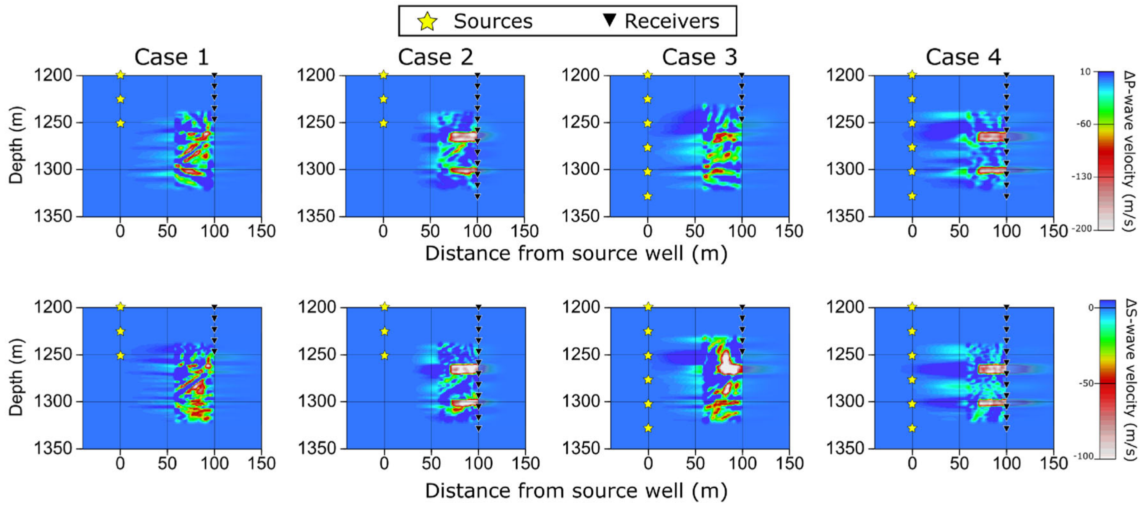

Figure 16
Comparison of the P- (top) and S-wave (bottom) velocity differences between the Baseline and the Monitor model across the four different acquisition geometries. The images depict the recovery of the model geometry and velocity magnitudes, highlighting the impact of acquisition setup on subsurface characterisation. The placement of the sources (yellow stars) and the receivers (black triangles) plays a crucial role in resolving velocity changes, with a couple of configurations leading to more accurate imaging of the deep reservoirs. FWI in Cases 2 and 4 leads to more pronounced velocity anomalies, indicating better sensitivity to subsurface variations

thicknesses. In contrast, the S-wave profile successfully identifies them, but still introduces an artificial layer in between. Lastly, the inversion results for Case 4 agree with the true models for both P- and S-wave velocities.

Monitoring velocity variations involves not only detecting changes but also their geometry. Figure 16 shows 2D differences in P- and S-wave velocities between Stages 4 and 6 for the four cases. Due to the significant degrees of freedom in Stage 6, the results are noisy, especially in Case 1, where the algorithm struggles to detect the reservoirs even before introducing variations.

Despite this, the P-wave velocity results reveal that the upper reservoir was consistently detected across all four geometries, although with varying accuracy. In Case 1, it is nearly masked by numerical noise (see Sect. 4.2.2), though high variations can be identified at the target depth. Case 3 also shows variations at the reservoir depth, but with artefacts between layers. Cases 2 and 4 successfully recover the geometry of the velocity changes, with Case 4 achieving a higher resolution.

The deepest reservoir presented greater challenges for the estimation of the P-wave velocity model. In Case 1, a layer with a larger extent and far from the well was detected, suggesting noise rather than a true signal. Case 2 recovered the correct extent, but with less definition than in the upper reservoir. Case 3 had similar sensitivity to the upper reservoir, but introduced an artificial layer. Case 4 accurately recovered the lower reservoir shape and extent of the changes.

the deepest reservoir geometry but introduces an artificial feature between and above the reservoirs. Despite this, it captures the correct horizontal extent of both anomalies, suggesting that with further constraints, it could generate more accurate results.

All acquisition geometries successfully detect the upper reservoir (10 m thick). However, sensitivity to the deeper reservoir (6 m thick) is more limited, with only Cases 2 and 4 recovering the geometry and the amplitude of the velocity changes. The high degrees of freedom in Stage 6, combined with limited sampling, numerical noise, and inversion instabilities, introduce numerical artefacts in some geometries. These limitations reinforce the importance of carefully designed acquisition and additional constraints to improve monitoring accuracy. The results also indicate that to monitor such changes effectively, it is crucial to position sources or receivers (if not both) across the target zones, with receivers near the injection depth providing the most reliable results.

5. Conclusions

This study investigated the feasibility of DAS-based crosswell Full Waveform Inversion (FWI) for detecting elastic parameter variations in deep georeservoirs caused by high-temperature storage. The DeepStor project was taken as a case study. Expected changes include a 7% decrease in the P- and S-wave velocities, and 1% increase in rock density within a 30 m radius around the injection/production well, at circa 1300 m depth, within layers with thicknesses of 10 m and 6 m. Four cross-well seismic surveys were analysed and compared to assess their ability to image changes between the Baseline and the Monitor datasets.

Processing strain along a vertical optic fibre proved sufficient to characterise reservoir properties and anomalies in most geometries. The FWI results demonstrate the importance of survey design in accurately imaging the changes. Geometries with DAS sampling points crossing the reservoir layers, such as in Cases 2 and 4, were most effective in resolving thin layers and detecting velocity changes. The best resolution was obtained for Case 4, with both sources and DAS sampling points crossing the reservoir zone. In contrast, Cases 1 and 3, where DAS sampling points did not cross the reservoir, showed greater sensitivity to the initial model and poorer inversion results, highlighting the importance of survey design and the associated deep wells for such monitoring purposes. However, all cases proved sensitive to the variations in velocity.

The six-stage FWI process successfully imaged baseline structures and anomalies in most cases. Incorporating constraints in the model space, such as spatial uncertainties and correlation ranges, improved inversion stability and resolution. More importantly, the inclusion of shear waves provided an additional parameter to constrain the inversion and enhanced the resolution and detection of thin reservoirs and their changes in properties, highlighting the importance of elastic modelling and the need for acquisition of elastic data in geothermal monitoring.

Future research should explore the impact of noise, attenuation and anisotropy, and assess whether a standard three-component geophone string would improve the results under realistic field conditions.

Acknowledgements

We thank the company Geophysical Inversion & Modeling-labs (GIM-labs) for providing the software and computational resources necessary for this research. We thank CYU and ISTeP for welcoming C.E.Fraile and the Karlsruhe House of Young Scientists (KHYS) for funding her research stay, which played a crucial role in enabling this study. This research is part of the subtopic ‘Geoenergy’ within the program ‘MTET - Materials and Technologies for the Energy Transition’ of the Helmholtz Association.

Author Contributions Conceptualization, C.E.F., E.G., C.B.; formal analysis, C.E.F., C.B.; funding acquisition, C.E.F.; investigation, C.E.F., C.B.; methodology, C.E.F., E.G., C.B.; resources, C.E.F., C.B.; software, C.B.; validation, C.E.F., C.B.; visualisation, C.E.F.; writing—original draft, C.E.F.; writing—review and editing, C.E.F., E.G., C.B. All authors read and approved the final manuscript.

Funding

Open Access funding enabled and organized by Projekt DEAL. C.E.Fraile received a research travel grant from the Karlsruhe House of Young Scientists (KHYS) to conduct research at CYU. This work is part of the program ‘MTET - Materials and Technologies for the Energy Transition’ of the Helmholtz Association.

Data Availability

No datasets were generated or analysed during the current study.

Declarations

Conflict of interest The authors have no relevant financial or non-financial interests to disclose.

References

Azzola, J., Thiemann, K., & Gaucher, E. (2023). Integration of distributed acoustic sensing for real-time seismic monitoring of a geothermal field. *Geothermal Energy, 11*(1), 30. https://doi.org/10.1186/s40517-023-00272-4

Banks, J., Poulette, S., Grimmer, J., Bauer, F., & Schill, E. (2021). Geochemical changes associated with high-temperature heat storage at intermediate depth: Thermodynamic equilibrium models for the DeepStor site in the upper rhine graben, Germany. *Energies, 14*(19), 6089. https://doi.org/10.3390/en14196089

Bjorlykke, K. (2010). *Petroleum geoscience: From sedimentary environments to rock physics*. Springer, Berlin Heidelberg.

Böcker, J. (2015). In *Petroleum system and thermal history of the upper rhine graben: Implications from organic geochemical analyses, oil-source rock correlations and numerical modelling* DissertationAachenRWTH Aachen. https://publications.rwth-aachen.de/record/572508

Bremer, J., Nitschke, F., Bauer, F., Schill, E., Kohl, T., Kaymacki, E., & Jahrfeld, T. (2022). VESTA - very-high-temperature heat aquifer storage. In *European geothermal congress 2022 proceedings*, Retrieved from https://europeangeothermalcongress.eu/wp763content/uploads/2024/10/EGC2022.pdf

Bunks, C., Saleck, F. M., Zaleski, S., & Chavent, G. (1995). Multiscale seismic waveform inversion. *Geophysics, 60*(5), 1457–1473. https://doi.org/10.1190/1.1443880. (Publisher: Society of Exploration Geophysicists).

Calvert, R. (2005). 4D Repeatability and the effects of heterogeneous overburden distortion and noise. In *Insights and methods for 4D reservoir monitoring and characterization.* USA: Society of Exploration Geophysicists and European Association of Geoscientists and Engineers. https://doi.org/10.1190/1.9781560801696

Cartagena-Pérez, D., Arias-Buitrago, J., Alzate-Espinosa, G., Arbelaez-Londoño, A., Morales-Monsalve, C., Araujo-Guerrero, E., & Naranjo-Agudelo, A. (2018). A modified model to describe porosity-temperature relationship. *Journal of Petroleum Science and Engineering, 168*, 301–309. https://doi.org/10.1016/j.petrol.2018.04.067

Charara, M., & Barnes, C. (2019). Constrained full waveform inversion for borehole multicomponent seismic data. *Geosciences, 9*(1), 45. https://doi.org/10.3390/geosciences9010045

Charara, M., Barnes, C., & Tarantola, A. (1996). Constrained waveform inversion of seismic well data. In B. H. Jacobsen, K. Mosegaard, & P. Sibani (Eds.), *Inverse methods: Interdisciplinary elements of methodology, computation, and applications* (pp. 98–112). Springer, Berlin Heidelberg.

Chen, S., Zhang, Q., Andrews-Speed, P., & Mclellan, B. (2020). Quantitative assessment of the environmental risks of geothermal energy: A review. *Journal of Environmental Management, 276*, 111287. https://doi.org/10.1016/j.jenvman.2020.111287

Cheng, F., Xia, J., Ajo-Franklin, J. B., Behm, M., Zhou, C., Dai, T., & Zhou, C. (2021). High-resolution ambient noise imaging of geothermal reservoir using 3c dense seismic nodal array and ultra-short observation. *Journal of Geophysical Research: Solid Earth*. https://doi.org/10.1029/2021JB021827

Cooper, J., Ratcliffe, A., & Poole, G. (2021). Mitigating cycle skipping in full-waveform inversion using partial matching filters. In *82nd eage annual conference & exhibition* (pp. 1–5). Amsterdam, The Netherlands: European Association of Geoscientists & Engineers. https://doi.org/10.3997/2214-4609.202010725

Cuny, T., Bettinelli, P., & Le Calvez, J. (2024). Variable gauge length: Processing theory and applications to distributed acoustic sensing. *Geophysical Prospecting, 73*(1), 160–187. https://doi.org/10.1111/1365-2478.13640. (Publisher: Wiley).

Dean, T., Cuny, T., & Hartog, A. H. (2017). The effect of gauge length on axially incident p-waves measured using fibre optic distributed vibration sensing. *Geophysical Prospecting, 65*(1), 184–193. https://doi.org/10.1111/1365-2478.12419. (Publisher: Wiley).

Doetsch, J., Gischig, V. S., Villiger, L., Krietsch, H., Nejati, M., Amann, F., & Giardini, D. (2018). Subsurface fluid pressure and rock deformation monitoring using seismic velocity observations. *Geophysical Research Letters*. https://doi.org/10.1029/2018GL079009

Drijver, B., van Aarssen, M., & de Zwart, B. (2012). High-temperature aquifer thermal energy storage (HT-ATES): sustainable and multi-usable. In *Proceedings of innostock 2012: The 12th international conference on energy storage.* Lleida, Spain.

Edwards, B., Kraft, T., Cauzzi, C., Kastli, P., & Wiemer, S. (2015). Seismic monitoring and analysis of deep geothermal projects in St gallen and basel switzerland. *Geophysical Journal International, 201*(2), 1022–1039. https://doi.org/10.1093/gji/ggv059

Fichtner, A. (2010). *Full seismic waveform modelling and inversion*. Springer. https://doi.org/10.1007/978-3-642-15807-0

Fraile, C., Kohl, T., & Gaucher, E. (2024). Estimation of seismic velocity changes in a HT-ATES system using THM modelling.

In *EGU General Assembly,2024*. https://doi.org/10.5194/egusphere-egu24-11143

Freymark, J., Sippel, J., Scheck-Wenderoth, M., Bär, K., Stiller, M., Fritsche, J. G., & Kracht, M. (2017). The deep thermal field of the upper rhine graben. *Tectonophysics, 694*, 114–129. https://doi.org/10.1016/j.tecto.2016.11.013

Furre, A.-K., Eiken, O., Alnes, H., Vevatne, J. N., & Kiær, A. F. (2017). 20 years of monitoring CO_2-injection at sleipner. *Energy Procedia, 114*, 3916–3926. https://doi.org/10.1016/j.egypro.2017.03.1523

Ganguly, S., & Mohan Kumar, M. S. (2012). Geothermal reservoirs—a brief review. *Journal of the Geological Society of India, 79*(6), 589–602. https://doi.org/10.1007/s12594-012-0098-8

Gardner, G. H. F., Gardner, L. W., & Gregory, A. R. (1974). Formation velocity and density—the diagnostic basics for stratigraphy traps. *Geophysics, 39*(6), 770–780. https://doi.org/10.1190/1.1440465

Hartog, A. H. (2017). *An introduction to distributed optical fibre sensors*. Taylor & Francis Group.

Hermans, T., Nguyen, F., Robert, T., & Revil, A. (2014). Geophysical methods for monitoring temperature changes in shallow low enthalpy geothermal systems. *Energies, 7*(8), 5083–5118. https://doi.org/10.3390/en7085083

Hunt, T. M., Bromley, C. J., Risk, G. F., Sherburn, S., & Soengkono, S. (2009). Geophysical investigations of the wairakei Field. *Geothermics, 38*(1), 85–97. https://doi.org/10.1016/j.geothermics.2008.11.002

Johannessen, K., Drakeley, B., & Farhadiroushan, M. (2012). Distributed acoustic sensing - a new way of listening to your well/reservoir. In *SPE intelligent energy international conference and exhibition* (pp. SPE–149602–MS). Utrecht, The Netherlands: Society of Petroleum Engineers. https://doi.org/10.2118/149602-MS

Lindsey, N. J., Rademacher, H., & Ajo-Franklin, J. B. (2020). On the broadband instrument response of fiber-optic DAS arrays. *Journal of Geophysical Research: Solid Earth*. https://doi.org/10.1029/2019jb018145

Lowrie, W. (1997). *Fundamentals of geophysics*. Cambridge University Press.

Lumley, D. E. (2001). Time-lapse seismic reservoir monitoring. *Geophysics, 66*(1), 50–53. https://doi.org/10.1190/1.1444921

Lutz, M., & Cleintuar, M. (1999). Bulletin: For applied geology (Tech. Rep.) Losone, Switzerland.: SASEG, Swiss Association of Petroleum Geologists and Engineers and SFIG, Swiss Group for Engineering Geology.

Matsushima, J., Yokota, T., Okubo, Y., Rokugawa, S., Tanaka, K., Tsuchiya, T., & Tani, K. (2004). Repeated seismic reflection measurements in the kakkonda geothermal field. *Journal of Volcanology and Geothermal Research, 129*(4), 343–356. https://doi.org/10.1016/S0377-0273(03)00286-5

Nocedal, J., & Wright, S. J. (2006). *Numerical optimization* (2nd ed.). Springer.

Ocłoń, P. (2021). *Renewable energy utilization using underground energy systems* (Vol. 84). Springer International Publishing. https://doi.org/10.1007/978-3-030-75228-6

Pladys, A., Brossier, R., Li, Y., & Métivier, L. (2021). On cycle-skipping and misfit function modification for full-wave inversion: Comparison of five recent approaches. *Geophysics, 86*(4), R563–R587. https://doi.org/10.1190/geo2020-0851.1

Podgornova, O., Bettinelli, P., Liang, L., Le Calvez, J., Leaney, S., Perez, M., & Soliman, A. (2022). Full-waveform inversion of fiber-optic VSP data from deviated wells. In: *SPWLA 63rd annual symposium transactions*. Stavanger, Norway: Society of Petrophysicists and Well Log Analysts. Retrieved from https://doi.org/10.30632/spwla-2022-0012

Pratt, R. G., Shin, C., & Hicks, G. J. (1998). Gauss-newton and full newton methods in frequency-space seismic waveform inversion. *Geophysical Journal International, 133*(2), 341–362. https://doi.org/10.1046/j.1365-246X.1998.00498.x

Rabbel, W., Jusri, T., Köhn, D., Bahadur Motra, H., Niederau, J., Schreiter, L., & Wuttke, F. (2017). Seismic velocity uncertainties and their effect on geothermal predictions: A case study. *Energy Procedia, 125*, 283–290. https://doi.org/10.1016/j.egypro.2017.08.178

Reinecker, J., Gutmanis, J., Foxford, A., Cotton, L., Dalby, C., & Law, R. (2021). Geothermal exploration and reservoir modelling of the united downs deep geothermal project, Cornwall (UK). *Geothermics, 97*, 102226. https://doi.org/10.1016/j.geothermics.2021.102226

Sambo, C., Iferobia, C. C., Babasafari, A. A., Rezaei, S., & Akanni, O. A. (2020). The role of time lapse(4D) seismic technology as reservoir monitoring and surveillance tool: A comprehensive review. *Journal of Natural Gas Science and Engineering, 80*, 103312. https://doi.org/10.1016/j.jngse.2020.103312

Schmelzbach, C., Greenhalgh, S., Reiser, F., Girard, J.-F., Bretaudeau, F., Capar, L., & Bitri, A. (2016). Advanced seismic processing/imaging techniques and their potential for geothermal exploration. *Interpretation, 4*(4), SR1–SR18. https://doi.org/10.1190/INT-2016-0017.1

Shewchuk, J.R. (1994). *An introduction to the conjugate gradient method without the agonizing pain* (11/4 ed.; Tech. Rep.). USA: School of Computer Science, CMU.

Sommer, W., Valstar, J., Leusbrock, I., Grotenhuis, T., & Rijnaarts, H. (2015). Optimization and spatial pattern of large-scale aquifer thermal energy storage. *Applied Energy, 137*, 322–337. https://doi.org/10.1016/j.apenergy.2014.10.019

Stober, I., & Bucher, K. (2021). *Geothermal energy: From theoretical models to exploration and development*. Springer International Publishing.

Stricker, K., Egert, R., Schill, E., & Kohl, T. (2024). Risk of surface movements and reservoir deformation for high-temperature aquifer thermal energy storage (HT-ATES). *Geothermal Energy, 12*(1), 4. https://doi.org/10.1186/s40517-024-00283-9

Stricker, K., Grimmer, J., Egert, R., Bremer, J., Korzani, M. G., Schill, E., & Kohl, T. (2020). The potential of depleted oil reservoirs for high-temperature storage systems. *Energies, 13*(24), 6510. https://doi.org/10.3390/en13246510

Tarantola, A. (1984). Inversion of seismic reflection data in the acoustic approximation. *Geophysics, 49*(8), 1259–1266. https://doi.org/10.1190/1.1441754

Virieux, J. (1984). SH-wave propagation in heterogeneous media: Velocity-stress finite-difference method. *Geophysics, 49*(11), 1933–1957. https://doi.org/10.1190/1.1441605

Virieux, J. (1986). P-SV wave propagation in heterogeneous media: Velocity-stress finite-difference method. *Geophysics, 51*(4), 889–901. https://doi.org/10.1190/1.1442147

Virieux, J., Asnaashari, A., Brossier, R., Métivier, L., Ribodetti, A., & Zhou, W. (2017). An introduction to full waveform inversion.

In: *Encyclopedia of exploration geophysics* (pp. R1-1–R1-40). USA: Society of Exploration Geophysicists. https://doi.org/10.1190/1.9781560803027.entry6

Virieux, J., & Operto, S. (2009). An overview of full-waveform inversion in exploration geophysics. *Geophysics, 74*(6), WCC1–WCC26. https://doi.org/10.1190/1.3238367

Winner, V. (2023). *Optimized Experimental design for seismic full waveform inversion* (Doctoral dissertation, ETH Zurich). https://doi.org/10.3929/ethz-b-000614505

Young, K., Reber, T., & Witherbee, K. (2012). Hydrothermal exploration best practices and geothermal knowledge exchange on OpenEI. In: *Thirty-seventh workshop on geothermal reservoir engineering*. Standford, USA.

(Received November 13, 2025, revised June 24, 2026, accepted July 1, 2026)